

Large-Enhancement Nanoscale Dynamic Nuclear Polarization Near a Silicon Nanowire Surface

Sahand Tabatabaei,^{1,2†} Pritam Priyadarsi,^{1,2†} Namanish Singh,^{1,2}
Pardis Sahafi,^{1,2} Daniel Tay,^{1,2} Andrew Jordan,^{1,2} Raffi Budakian^{1,2*}

¹Department of Physics and Astronomy, University of Waterloo, Waterloo, ON, Canada, N2L3G1

²Institute for Quantum Computing, University of Waterloo, Waterloo, ON, Canada, N2L3G1

*To whom correspondence should be addressed; E-mail: rbudakian@uwaterloo.ca.

† These authors contributed equally to this work.

Dynamic nuclear polarization (DNP) has revolutionized the field of NMR spectroscopy, expanding its reach and capabilities to investigate diverse materials, biomolecules, and complex dynamic processes. Bringing high-efficiency DNP to the nanometer scale would open new avenues for studying nanoscale nuclear spin ensembles, such as single biomolecules, virus particles, and condensed matter systems. Combining pulsed DNP with nanoscale force-detected magnetic resonance measurements, we demonstrated a 100-fold enhancement in the Boltzmann polarization of proton spins in nanoscale sugar droplets at 6 K and 0.33 T. Crucially, this enhancement corresponds to a factor of 200 reduction in the averaging time compared to measurements that rely on the detection of statistical fluctuations in nanoscale nuclear spin ensembles. These results significantly advance the capabilities of force-detected magnetic resonance detection as a practical tool for nanoscale imaging.

Introduction

Nuclear magnetic resonance (NMR) plays a pivotal role in modern science and technology, with applications ranging from characterizing molecular structure and dynamics, to studying complex systems in condensed matter physics and advancing diagnostic imaging in medicine. In recent decades, extensive research has gone into bringing the powerful capabilities of magnetic resonance, particularly magnetic resonance imaging (MRI), to the nanometer scale (1–14). The primary goal of these efforts – collectively called nanoscale MRI (nanoMRI) – is to achieve three-dimensional angstrom-resolution imaging of macromolecules and nanoscale molecular complexes, with a keen focus on biologically significant samples, such as proteins and virus particles whose characteristic length scale is of order (100 nm)³. In recent years, significant advancements in detection sensitivity have been made through the development of more sensitive spin sensors. This progress ranges from the fabrication of ultra-low dissipation nanomechanical cantilevers (15–17) and high gradient magnets in force-detected platforms (18, 19), to improved coherence times and surface properties of shallow nitrogen-vacancy (NV) quantum sensors (20–22). While these approaches show promise, substantial progress is still needed to fully realize nanoMRI’s potential as a non-destructive and chemically-selective tool for studying nanoscale nuclear spin systems at atomic length scales.

Owing to the small nuclear spin polarization, even at high field and cryogenic conditions, NMR has been plagued by low detection signal-to-noise ratio (SNR). Since its inception, numerous techniques have been devised for enhancing the nuclear spin polarization in NMR (23). Among these, dynamic nuclear polarization (DNP) (24–26) enhances the signal by transferring the larger polarization of unpaired electrons, in either thermally, optically, or chemically polarized states, to nearby nuclei via hyperfine couplings. DNP can boost the detection sensitivity of nuclei by a factor of $\gamma_e/\gamma_n \geq 658$ relative to the signal obtained from thermal polarization,

where γ_e and γ_n are the electron and nuclear gyromagnetic ratios, respectively. Such signal enhancements have shortened acquisition times by several orders of magnitude and dramatically expanded the horizons of NMR spectroscopy and imaging (27–36).

The integration of DNP methods into nanoMRI marks a significant milestone towards the goal of nanoscale imaging of proteins and virus particles. However, achieving an SNR advantage with DNP in nanoscale systems is challenging because, as shown in Fig. 1, for typical spin populations in nanoscale volumes, statistical fluctuations in the number of up vs. down spins is often much larger than the Boltzmann polarization that is commonly measured in NMR. Furthermore, a collection of spins is always “statistically-polarized”, and hence can be continuously measured, whereas a measurement of the Boltzmann polarization requires waiting a time of order the spin-lattice relaxation time T_1 for the spin ensemble to reach thermal equilibrium. Therefore, most nanoscale force-detected NMR protocols do not measure thermal polarization, but instead rely on the detection of the statistical polarization (37–39). For DNP to yield an SNR advantage, it must not only boost the average polarization to a level that is larger than the statistical polarization, but also account for the higher acquisition rate of the statistically-polarized signal.

In this work, we present force-detected pulsed DNP measurements of proton spins in nanoscale droplets containing the trityl-OX063 free radical dissolved in water sugar mixtures. We demonstrate enhancements of thermal polarization exceeding 100 at 6 K and 0.33 T. Importantly, we achieve a 15-fold increase in the detection SNR of hyperpolarized vs. statistically-polarized protons for a sample volume of $\sim (250 \text{ nm})^3$, corresponding to a 200-fold decrease in the signal acquisition time. We find that the observed enhancements are facilitated by increased spin-lattice relaxation rates of OX063 electron spins caused by spin diffusion to fast-relaxing paramagnetic defects on the surface of the silicon nanowire (SiNW) force sensor. Numerical simulations of this process, provided in the Supplementary Materials, offer insights into opti-

mizing the DNP efficiency in future experiments. Our results represent a transformative step towards bringing the large sensitivity enhancements of DNP to nanoMRI measurements, paving the way for a practical NMR platform for performing three-dimensional nanoscale nuclear spin imaging.

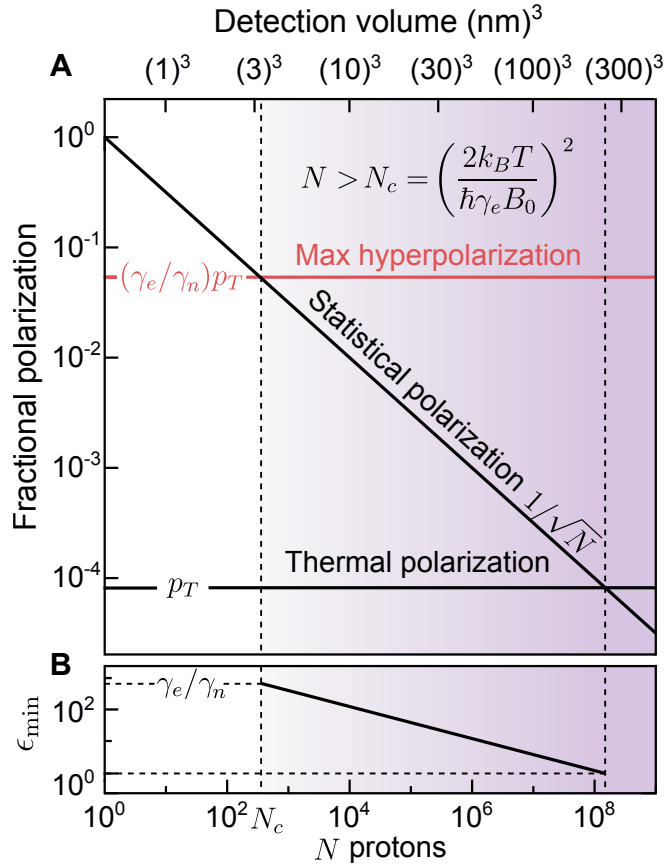


Figure 1: Comparison of Thermal, Statistical and DNP-Enhanced Fractional Polarizations in Nanoscale Spin Ensembles. (A) Calculated fractional polarizations for N proton spins at $T = 4.2$ K and $B_0 = 0.32$ T. The thermal polarization $p_T = \hbar \gamma_n B_0 / (2k_B T) = 7.78 \times 10^{-5}$ can be enhanced by a maximum factor of $\gamma_e / \gamma_n = 658$ (red line) through polarization transfer from electrons in a thermal state. A potential increase in SNR via DNP can be expected for $N > N_c$ (shaded region), where $N_c = \left(\frac{2k_B T}{\hbar \gamma_e B_0} \right)^2 = 382$. The top axis is calculated using a representative proton density of 1×10^{10} m⁻³ for organic samples, such as the tobacco mosaic virus (TMV) particle (1). (B) The minimum enhancement ϵ_{\min} for DNP to surpass statistical polarization. For the example of the TMV particle occupying a $\sim (50 \text{ nm})^3$ volume, $\epsilon_{\min} \sim 10$.

Results

Experimental Setup

Fig. 2A depicts our experimental setup, which is similar to the one used in our previous experiments (10, 13). Force-detected magnetic resonance measurements were performed on samples consisting of a droplet of a water/ethanol/sugar solution attached to the tip of a SiNW nanomechanical resonator. Four different samples were measured, with each droplet ranging from 150 nm to 300 nm in diameter. The samples contained varying concentrations of the trityl-OX063 electron free radical used for the DNP measurements. The exact description of each sample is provided in Materials and Methods (Table 2). After attachment, the samples were mounted to the force microscope and kept under high vacuum for several days prior to cooling down to 4.2 K. Noise thermometry measurements showed an increase in the sample temperature between 1 K to 2 K caused by absorption of 1510 nm light used for interferometric displacement detection of the SiNW – a known effect in our platform (10). For details regarding sample preparation and noise thermometry measurements, see the Supplementary Materials.

DNP measurements were conducted in an external field of 0.33 T, applied parallel to the SiNW axis. The proton ($I = 1/2$) and electron ($S = 1/2$) Larmor frequencies at this field were $\omega_{0I}/(2\pi) = 14.1$ MHz and $\omega_{0S}/(2\pi) = 9.26$ GHz, respectively. A current focusing field gradient source (CFFGS) was utilized to generate the time-dependent magnetic fields and magnetic field gradients needed for spin control and detection (see Materials and Methods). The tip of the sample was aligned to the center of the CFFGS and positioned 100 nm above the surface. The transverse field $B_1 = \sqrt{B_x^2 + B_y^2}/2$ used to excite magnetic resonance was generated by driving the CFFGS at the Larmor frequency of the targeted spin, where B_x , B_y , B_z are the magnetic field components. The B_1 field generated was highly non-uniform and varied by a factor of ~ 2.5 over the sample volume. The maximum peak current applied to the CFFGS for

proton and electron control was 29 mA and 6 mA, respectively. For further details regarding the CFFGS field profile, see the Supplementary Materials.

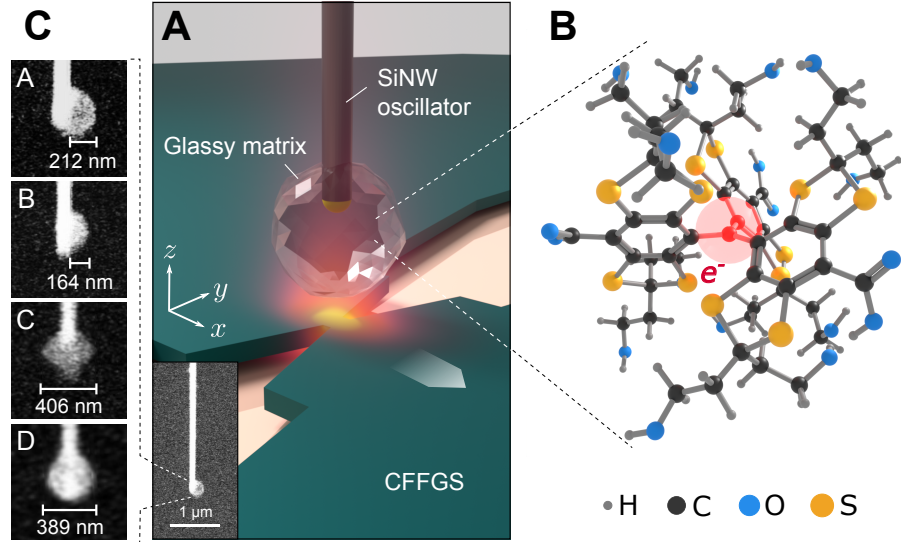


Figure 2: Experimental Setup and Polarizing Agent. (A) Schematic of the experimental setup, including the SiNW force sensor, CFFGS, and the sample comprised of polarizing agents in a glassy sugar matrix. (Inset) Scanning electron microscope (SEM) image of sample A attached to a SiNW. (B) The trityl-OX063 radical used as a polarizing agent, with the unpaired electron indicated in red. The radical’s highly symmetric structure is known to yield an exceptionally small linewidth and g-anisotropy (40). (C) SEM images of each of the measured nanodroplets.

DNP Protocol

Our measurements utilize the nuclear orientation via electron spin-locking (NOVEL) DNP protocol—a fast and highly efficient method for polarization transfer (26, 41, 42). For efficient polarization transfer that is robust to the spatial variation of the electron Rabi frequency $\omega_{1S} = \gamma_e B_1$ in our setup, we utilized a modified version of the ramped-amplitude NOVEL (RA-NOVEL) protocol (41). The protocol (Fig. 3A) starts by tipping the electron spins into the transverse plane with an adiabatic half passage (AHP) pulse, and applying a resonant spin-locking drive, whose amplitude is linearly swept to zero in a time T_{ramp} . The Hamiltonian of

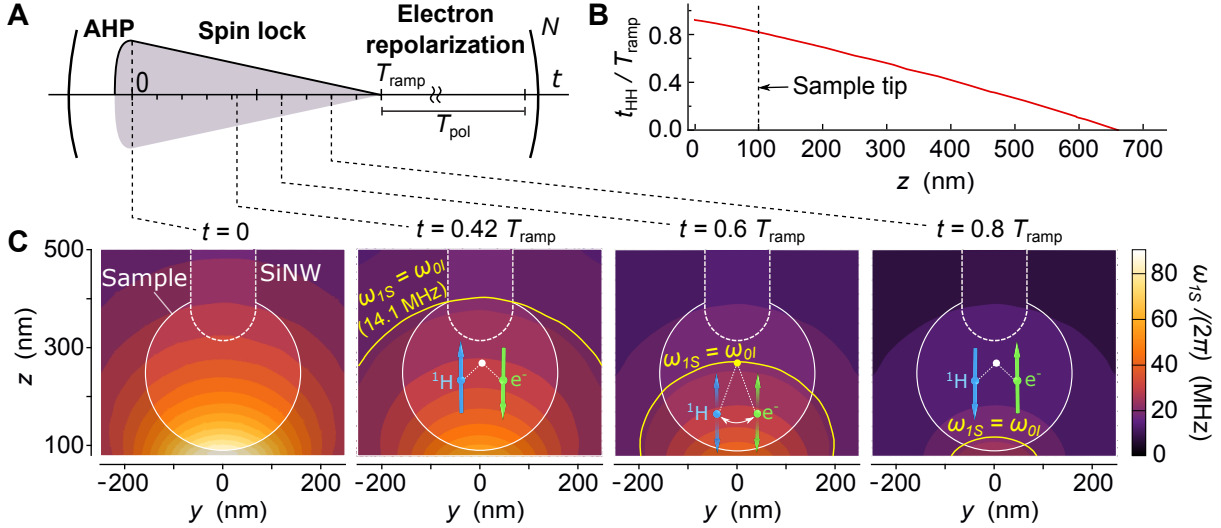


Figure 3: **RA-NOVEL Protocol.** (A) RA-NOVEL waveform applied to electrons, consisting of an adiabatic half passage (AHP), ramped-amplitude spin-locking pulse and electron repolarization period T_{pol} . Repetitions of this primitive allow for successive build-up of proton polarization up to a time of order the proton spin-lattice relaxation time T_{1p} . (B) The time t_{HH} at which an electron-proton pair at distance z from the CFFGS undergoes the Hartmann-Hahn condition $\omega_{1S} = \omega_{0I}$. The plot is calculated along the center of the CFFGS ($x = y = 0$). (C) ω_{1S} contours at different instances in the ramp. An electron-proton spin pair (white dot) undergoes an adiabatic exchange of polarization as ω_{1S} is swept past the Hartmann-Hahn condition (yellow contour). The arrows indicate the two-spin state in the tilted rotating frame. The polarization transfer begins away from the CFFGS and moves towards it as the ramp progresses.

a proton-electron spin pair in the electron's rotating frame is $H(t) = -\omega_{0I}I_z - \omega_{1S}(t)S_x - (A_0I_z + A_1I_x)S_z$, where A_0 and A_1 are the secular and pseudo-secular hyperfine couplings, respectively. For protons in the OX063 molecule, we expect $A_1/(2\pi) \sim 1$ MHz (43), while the coupling to protons in the surrounding matrix will depend on their local concentration and spatial distribution. A rotation of the reference frame around the y axis by $-\pi/2$, followed by perturbative truncation results in the polarization transfer Hamiltonian

$$\tilde{H}(t) = -\omega_{0I}I_z - \omega_{1S}(t)S_z - A_1(I_+S_- + I_-S_+)/2 \quad (1)$$

in the tilted rotating frame (41), where $I_{\pm} = I_x \pm iI_y$ and $S_{\pm} = S_x \pm iS_y$ are spin ladder operators. For an electron spin satisfying $\omega_{1S}(0) \gg \omega_{0I}$, an amplitude ramp that is sufficiently

slow relative to A_1 induces polarization exchange as ω_{1S} passes through the Hartmann-Hahn resonance $\omega_{1S}(t) = \omega_{0I}$. This occurs via the adiabatic evolution of the \tilde{H} eigenstates from $|\uparrow\downarrow\rangle$ to $|\downarrow\uparrow\rangle$ (and vice versa), with $|\downarrow\downarrow\rangle$ and $|\uparrow\uparrow\rangle$ left invariant. Fig. 3C illustrates this process at an arbitrary position in the CFFGS field distribution. Successive build-up of the polarization can be achieved by repeated application of the RA-NOVEL waveform primitive, while including a wait time T_{pol} in between the field sweeps to allow for the electrons to re-polarize, and the enhanced proton polarization to diffuse through the sample.

DNP Measurements

We measured the performance of RA-NOVEL using the pulse sequence shown in Fig. 4A. After initially scrambling the thermal proton polarization, N repetitions of the RA-NOVEL waveform were applied over a build-up time $T_b = N(T_{\text{ramp}} + T_{\text{pol}})$, and the average proton polarization was measured using the modulated alternating gradients generated with currents (MAGGIC) spin detection protocol. We refer to the Supplementary Materials and Ref. (10, 13) for details regarding the MAGGIC protocol. The MAGGIC protocol couples the average longitudinal (z axis) spin polarization to the mechanical motion of the SiNW via the time-dependent force $F(t) \propto e^{-t/\tau_m} \int d^3r n(\mathbf{r})G(\mathbf{r})m_0(\mathbf{r})$, resonant with the SiNW force sensor. Here, $G(\mathbf{r}) = \partial B_z(\mathbf{r})/\partial y$ is the peak amplitude of the detection gradient, $n(\mathbf{r})$ is the spin density, τ_m is the spin correlation time under MAGGIC, and $m_0(\mathbf{r})$ is the average polarization of a spin at position \mathbf{r} at the start of the measurement. We construct the average measured force $\bar{F} = \int_0^{\tau_0} dt w(t)F(t)$ for a given time record $F(t)$, where τ_0 is the measurement duration and $w(t)$ is a matched filter kernel determined for optimal SNR (see Supplementary Materials).

We quantify the DNP enhancement as the ratio $\eta(T_b, T_{\text{pol}}, T_{\text{ramp}}) = \bar{F}_{\text{hp}}(T_b, T_{\text{pol}}, T_{\text{ramp}})/\bar{F}_{\text{th}}(T_b)$, where we compare the hyperpolarized signal $\bar{F}_{\text{hp}}(T_b, T_{\text{pol}}, T_{\text{ramp}})$ with the thermal signal $\bar{F}_{\text{th}}(T_b)$ acquired from thermally-polarized protons for the same duration T_b . In the main text, we focus

on the data for sample A, while providing a summary for all samples in Table 1, and referring to the Supplementary Materials for complete data sets. Fig. 4B shows the measured time records $F(t)$ with and without DNP. The hyperpolarized and thermal signals were acquired with 8 min and 17.5 h of averaging, respectively. The optimum DNP buildup time $T_{b,\text{opt}}$ was determined by measuring the time constant τ_{DNP} of the DNP buildup (Fig. 4A(inset)) and choosing the value of T_b that maximized the detection SNR $\propto \sqrt{N_{\text{avg}}}(1 - e^{-T_b/\tau_{\text{DNP}}})$. Here, $N_{\text{avg}} = T_e/T_b$ is the number of averages during the total experiment duration T_e . For the measurements shown in Fig. 4, $\tau_{\text{DNP}} = 6.7(1)$ s and $T_{b,\text{opt}} = 7.7$ s. The optimum DNP parameters were found by measuring η for different values of T_{pol} and T_{ramp} with $T_b = T_{b,\text{opt}}$ held constant. The measured data (Fig. 4C) shows two qualitative features of the DNP process. First, the maximum value of η increases with increasing T_{ramp} , until either T_{ramp} exceeds the time scale set by the hyperfine coupling, or it approaches the electron spin-lattice relaxation time in the rotating frame $T_{1\rho e}$. Second, there is a trade-off between allowing enough time for electron re-polarization (governed by the electron spin-lattice relaxation time T_{1e}) and maximizing the number of DNP repetitions within the available buildup time T_b . For this sample, with $T_{1e} = 20.5(3)$ ms, a maximum enhancement of $\eta_{\text{opt}} = 105(8)$ was achieved for $T_{\text{pol,} \text{opt}} = 10.24$ ms and $T_{\text{ramp,} \text{opt}} = 16$ μ s. The ramp time $T_{\text{ramp,} \text{opt}}$ was 1-2 orders of magnitude lower than $T_{1\rho e}$ for all samples, indicating that $T_{\text{ramp,} \text{opt}}$ was set by the timescale of the pseudo-secular hyperfine coupling. We provide a semiclassical model for the DNP enhancement in the Supplementary Materials.

Previous force-detected DNP measurements of proton spins performed at 4.2 K and 0.6 T have obtained enhancements between 10-20 (44). The DNP efficiency in these measurements may have been limited by the significant magnetic field inhomogeneity generated by the permanent magnets utilized in these studies, potentially hindering spin diffusion among proton spins. A distinguishing feature of our measurement platform is the use of the CFFGS, which permits full temporal control of the detection gradient and the control fields applied to the spins. The

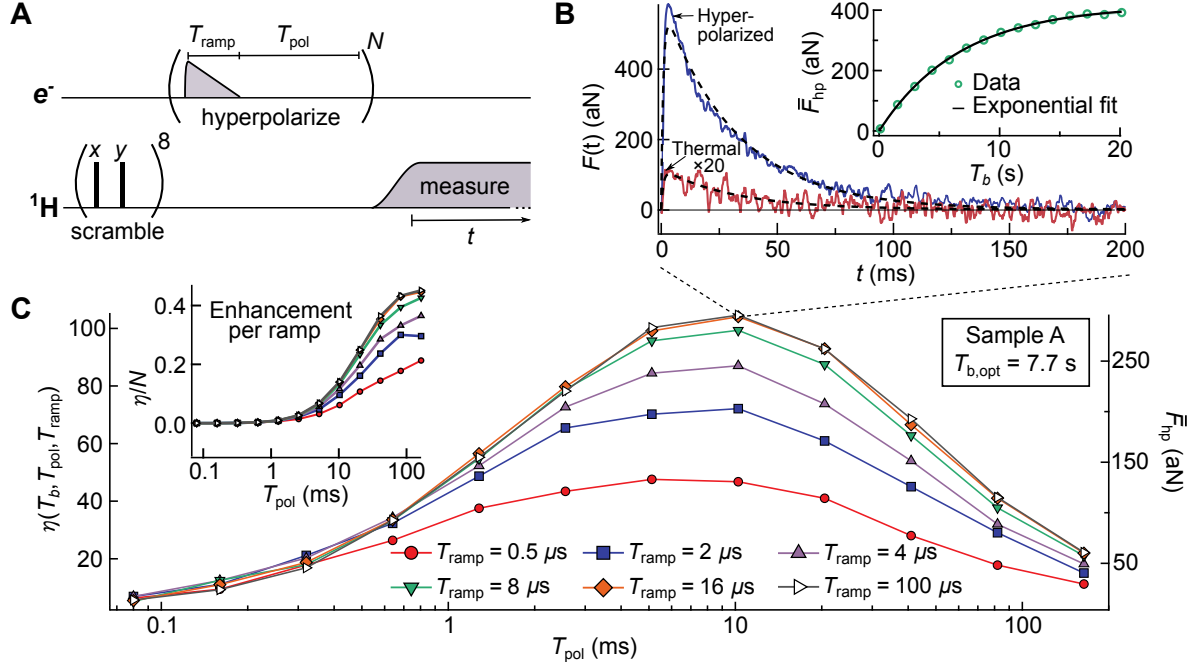


Figure 4: **Nanoscale DNP.** (A) DNP measurement sequence. The proton polarization is scrambled using a combination of $\pi/2_x$ and $\pi/2_y$ pulses with a dephasing time in between. DNP is then carried out by successive repetitions of the RA-NOVEL primitive for a build-up time T_b . (B) Measured hyperpolarized and thermal time records for sample A. The thermal measurement is done using the pulse sequence of (A) with the DNP waveform amplitude set to zero. A fit model to the mechanical response of the SiNW (dashed black lines) indicates a proton correlation time $\tau_m = 31.9(2)$ ms during the MAGGIC signal acquisition period (see Supplementary Materials). (Inset) Enhanced signal as a function of build-up time. (C) Measured enhancement as a function of T_{pol} and T_{ramp} , for a DNP buildup time of $T_{b,\text{opt}} = 7.7$ s. (Inset) The data is processed into the enhancement per ramp, depicting saturation of the enhancement with increasing T_{pol} and T_{ramp} . The error bars in the data are smaller than the plot marker size.

ability to turn off the large static field gradient during the DNP process may have contributed to the larger enhancements obtained in our measurements.

Table 1: Summary of nanoscale DNP results, including measured DNP performance metrics and spin relaxation times. See the Supplementary Materials for details of the relaxation time measurements.

	Sample	A	B	C	D
DNP performance	η_{opt}	105(8)	118(8)	78(3)	40.6(4)
	τ_{DNP} (s)	6.7(1)	0.67(1)	8.4(2)	14.9(5)
	$T_{b,\text{opt}}$ (s)	7.7	0.8	10.5	20.8
	$T_{\text{pol,} \text{opt}}$ (ms)	10.24	1.28	10.24	5.12
	$T_{\text{ramp,} \text{tabopt}}$ (μs)	16	8	16	100
Relaxation times	T_{1p} (s)	10.2(3)	1.01(3)	10.8(6)	20(1)
	$T_{1\rho e}$ (ms)	2.5(1)	0.45(4)	3.5(1)	7.5(3)
	T_{1e} (ms)	20.5(3)	2.5(1)	28.6(7)	30.0(4)

Comparison of DNP-Enhanced and Statistical Polarization SNR

To quantify the improvement in detection sensitivity provided by DNP relative to statistical polarization, we measured the proton Rabi distribution by using the B_1 gradient generated by the CFFGS to phase encode the proton spins. Following the Fourier-encoding scheme presented in Ref. (10, 13), time-domain signals were acquired, with and without prior hyperpolarization, after applying 10 μs long resonant pulses to the proton spins. The amplitude I_{pk} of the encoding pulses were varied between 0 mA to 29 mA in 17 steps and the spin signal was recorded as a function of the effective encoding time $\tau = 10 \mu\text{s} \times I_{\text{pk}}/I_0$, with $I_0 = 29 \text{ mA}$. Fig. 5 shows the SNR comparison for sample A. Prior to the acquisition of the DNP data, protons were hyperpolarized for 7.7 s by applying 752 repetitions of the DNP waveform, with $T_{\text{ramp}} = 16 \mu\text{s}$ and $T_{\text{pol}} = 10.24 \text{ ms}$. After hyperpolarization, the proton signal was acquired for 400 ms. Each data point, shown by the open circles in Fig. 5C, represents the average of two such measurements, corresponding to a total measurement time of 16.3 s. The statistically-polarized data was

obtained by continuously acquiring the spin signal for 16.1 s, calculating the average force in 100 ms long blocks of data acquired before and after the application of the 10 μ s long resonant pulse, and calculating the average correlation of two consecutive measurements; the average correlation is indicated by the open circles in Fig. 5A.

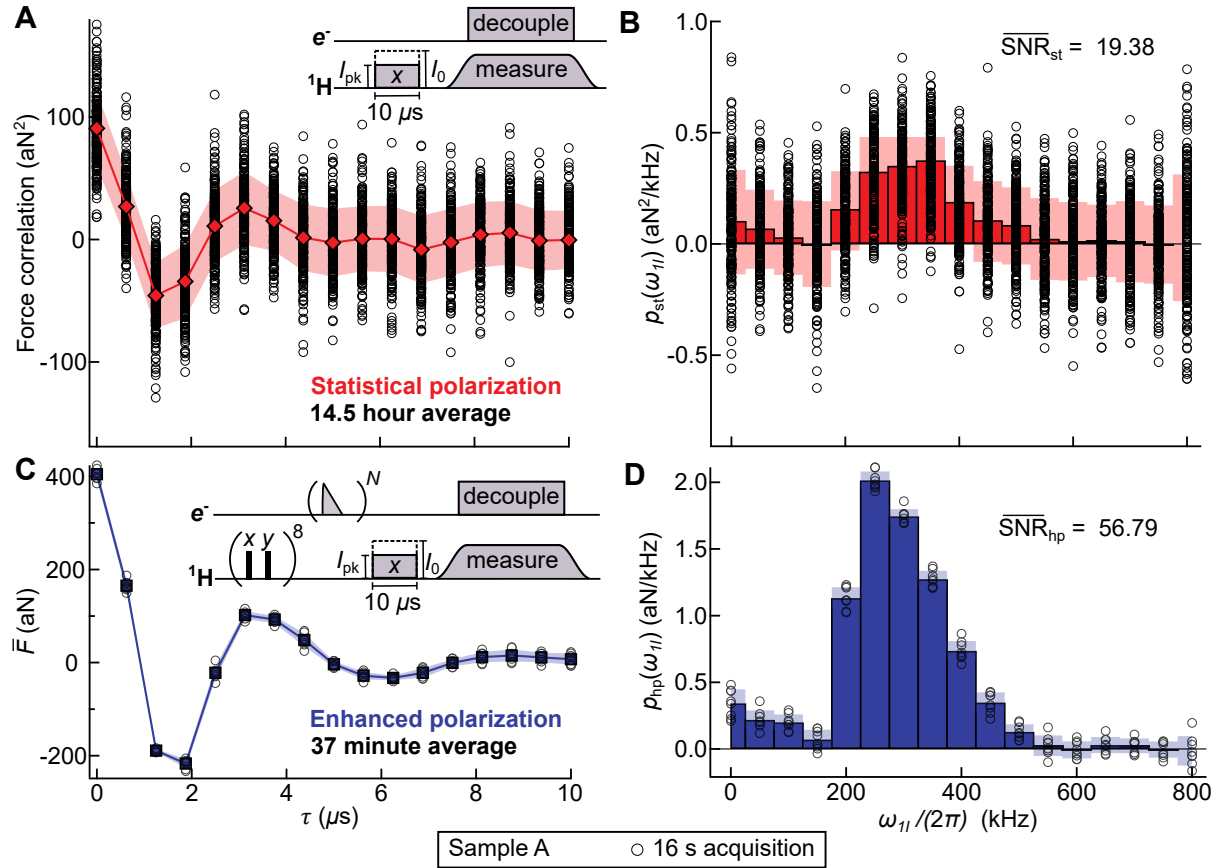


Figure 5: DNP-Enhanced and Statistical Polarization SNR Comparison. Measured time-domain Fourier encoding data for (A) statistically-polarized and (C) hyperpolarized proton spins in sample A. The corresponding Rabi frequency distributions are shown in (B) and (D). The frequency resolution of each distribution is 50 kHz. The shaded regions indicate the standard deviation of the acquired data (open circles) for each point in the time record, and the corresponding Rabi frequency distributions. The insets show the pulse sequence used for the two types of measurement. A constant amplitude excitation was applied at ω_{0S} to decouple the electrons while acquiring the proton signal. The decoupling procedure resulted in extending the proton spin correlation time from 31.9 ms to 135.6 ms during the acquisition period.

The solid lines in Fig. 5A,C represent the average of 192 (statistical) and 8 (hyperpolarized) data points measured for each value of τ . The averages shown correspond to a total measurement time of 14.5 h (statistical) and 37 min (hyperpolarized). Denoting the measured Rabi-frequency distribution and its standard deviation by $p(\omega_{1I})$ and $\sigma_p(\omega_{1I})$, respectively, we define the average SNR as $\overline{\text{SNR}} = \sum_{i=1}^{17} p(\omega_i) \text{SNR}_i / \sum_{i=1}^{17} p(\omega_i)$, where ω_i is the i^{th} Rabi frequency bin and $\text{SNR}_i = p(\omega_i) / \sigma_p(\omega_i)$. We determine $\overline{\text{SNR}}_{\text{st}} = 19.38$ and $\overline{\text{SNR}}_{\text{hp}} = 56.79$ for the statistical and hyperpolarized data, respectively, revealing a reduction in averaging time by a factor of $(\overline{\text{SNR}}_{\text{hp}} / \overline{\text{SNR}}_{\text{st}})^2 \times (14.5 \text{ h} / 37 \text{ min}) = 204$ to achieve equal average SNRs. Identical measurements on sample C, presented in the Supplementary Materials, indicate a similar 189-fold reduction in averaging time. A theoretical comparison of SNR for statistical and hyperpolarized measurements is provided in the Supplementary Materials.

Surface-Induced Electron Spin Relaxation

The electron spin-lattice relaxation time T_{1e} plays an important role in the DNP process, as it sets an upper bound on the repetition rate of the DNP waveform. A previous study conducted with bulk OX063 samples at 6 K for concentrations between 1 mM to 60 mM observed T_{1e} values ranging from 7 s to 50 ms (45). The primary relaxation mechanism in these studies was attributed to cross-relaxation with a small number of fast-relaxing OX063 aggregates in the solution. We find the T_{1e} values measured in nanoscale sugar droplets at the same temperature and over a similar concentration range of 1.3 mM to 49.4 mM to be substantially shorter than these previous studies, varying between 70 ms to 2.5 ms. Moreover, we find that the value of T_{1e} for samples prepared from the same solution on two different SiNWs can vary by more than a factor of 10.

In investigating the possible sources that could account for the shorter relaxation times, we first measured the thermal electron spin polarization as a function of the SiNW temperature.

For these studies, we used a 1.3 mM concentration reference sample, which had the longest relaxation time ($T_{1e} = 70$ ms) of all the samples we measured, and therefore should exhibit the highest sensitivity to extrinsic relaxation mechanisms. As seen in Fig. S7B of the Supplementary Materials, the thermal polarization varies inversely with the temperature of the SiNW, consistent with the Curie-Weiss Law, indicating that the additional relaxation mechanism is in thermal equilibrium with the SiNW. This observation rules out non-thermal sources of noise, e.g., excess noise from the microwave amplifiers, as the cause for the enhanced T_{1e} relaxation.

Previous studies conducted with nitrogen-vacancy (NV) centers have shown that Johnson noise caused by the thermal motion of electrons in a metal can lead to faster spin-lattice relaxation rates (46). To see whether the proximity to the CFFGS had an effect, we measured T_{1e} as a function of the distance from the CFFGS. Our measurements (Fig. S8 of the Supplementary Materials) show no variation over a large range of tip-surface distances between 50 nm to 500 nm, thus ruling out this effect. For details of the T_{1e} vs. distance and spin thermometry measurements, see the Supplementary Materials.

Finally, it is known that the Si/SiO₂ interface contains fast-relaxing paramagnetic defects (dangling bonds) (47, 48), where the defect surface density σ_d can vary from 10^{12} cm⁻² to 10^{13} cm⁻² (49–52), and where the defect spin-lattice relaxation time has been measured to be of order $T_{1d} \approx 40$ μ s at 4 K (52). To investigate the role played by paramagnetic defects, we conducted semi-classical simulations of spin diffusion, wherein electron spins on the surface of the SiNW and the OX063 were evolved probabilistically according to their dipole-dipole interactions (53), accounting for the sample geometry, electron spin lineshape, and surface defect density. We find that for simulations that assume $T_{1d} = 50$ μ s and $\sigma_d = 1 \times 10^{13}$ cm⁻², the calculated and measured T_{1e} values for the OX063 spins are consistent with each other (see Supplementary Materials Section 11). Interestingly, the simulations also reveal that the average relaxation rate of the OX063 spins can be very sensitive to the shape of the droplet and its

placement on the SiNW, consistent with our observations. Simulations conducted for samples B and C, which were prepared using the same stock solution, reproduce the factor of 10 variation in T_{1e} observed in the measurements. The variation is attributed to sample B being smaller and having a larger contact area with the SiNW, whereas sample C is somewhat larger, with the SiNW having minimal entry into the droplet (Fig. 2C). Our simulations point to cross relaxation among paramagnetic defects on the surface of the SiNW and the OX063 spins as the dominant source for the reduction in T_{1e} observed in our measurements.

Discussion

We have demonstrated large sensitivity enhancements in proton spin measurements by integrating high efficiency pulsed DNP into a force-detected nanoMRI platform. Utilizing this enhanced polarization, we have achieved a 204-fold reduction in acquisition time in measuring the proton Rabi frequency distribution relative to measurements using statistical polarization. Our findings suggest that the enhanced spin relaxation caused by defect spins on the SiNW surface significantly reduces the T_{1e} of the OX063 electron spins at 6 K and 0.33 T, contributing to the large DNP enhancements observed in this work. Previous DNP measurements conducted at 1.4 K and 2.35 T with silicon microparticles (54) have demonstrated that spin diffusion to a silicon surface, and subsequent relaxation via paramagnetic defects can lead to an increase in DNP enhancement. In a similar manner, it should be possible to further exploit the rapid spin relaxation caused by proximity to the SiNW surface to maintain large DNP enhancement at lower temperatures and higher magnetic fields.

In addition to the large sensitivity enhancement, our results are also notable as a demonstration of the versatility of our nanoMRI setup. We demonstrate that it is possible to control and measure both electron and proton spins in the same setup – a significant advancement over previous work (10) where measurements were performed only on proton spins. Furthermore,

we demonstrate the ability to reproducibly perform sample attachment with nanoscale droplets on the SiNWs. We envision that similar methods can be used to load other biologically relevant molecules e.g., proteins or virus particles, to our nanoMRI setup.

While these results already mark a transformative capability in nanoMRI detection, there remains significant room for improvement. Pulsed DNP schemes such as RA-NOVEL are known for their efficiency at high magnetic fields (24, 43). Extending our experiments to higher fields and sub-Kelvin temperatures could usher a fundamentally new regime for nuclear spin detection sensitivity. For example, polarization transfer with the same efficiency at 1 T and 0.3 K would lead to a factor of 400 SNR improvement compared to the detection of statistical polarization — a pivotal advance that would unlock unprecedented opportunities for probing nanoscale nuclear spin systems with near-atomic resolution.

Materials and Methods

SiNW Resonator

SiNW arrays were epitaxially grown on a Si(111) substrate with dimensions $1.5\text{ mm} \times 1\text{ mm} \times 0.4\text{ mm}$, using the vapor-liquid-solid method with a patterned array of Au catalyst particles near the edge of the chip. The growth environment consisted of H_2 and HCl gases with a SiH_4 precursor. The resulting SiNWs were $18\text{ }\mu\text{m}$ long with a diameter of 120 nm (17). The Au catalyst was removed using a KI solution to prevent the interaction of the Au particle with the electromagnetic fields generated by the CFFGS. Before sample attachment, the frequency of the fundamental flexural mode of the SiNWs ranged from 300 kHz to 600 kHz . The frequency decreased by $50\text{-}100\text{ kHz}$ after attachment of the sugar droplets, due to mass loading. After sample attachment, the quality factor of the SiNWs was $\sim 30,000$ at 4 K . To increase the measurement bandwidth of the resonator, a feedback signal was applied to a piezoelectric transducer glued to the SiNW chip, which effectively reduced the quality factor to 900 (55).

Sample Preparation and Attachment

The stock solutions used for sample preparation are given in Table 2. Droplets of the solution were attached to the SiNWs under an optical microscope using a micro-manipulator setup with a pneumatic injector. For details of the attachment process, see the Supplementary Materials. Scanning electron microscope images of the samples are depicted in Fig. 2C. Due to the uncertainty in water retention within the nanodroplet at 4 K and high-vacuum, exact calculation of the final OX063 concentrations is unfeasible. Accordingly, a concentration range is provided in Table 3, with the water content ranging from 0 to 100% of the initial solution. Ethanol was added to the water sugar mixture to reduce the surface tension and facilitate penetration of the SiNW into the solution. The ethanol is assumed to have fully evaporated under experimental conditions.

Table 2: Stock solutions used for sample preparation.

Sample	Stock Solution
A	0.9 M d ₁₂ -glucose/0.1 M glucose/2.1 mM OX063 in H ₂ O/D ₂ O/d ₆ -ethanol (1/9/10, v/v/v)
B, C	0.9 M d ₁₂ -glucose/0.1 M glucose/5.9 mM OX063 in H ₂ O/D ₂ O/d ₆ -ethanol (1/9/10, v/v/v)
D	1.2 M sucrose/7.3 mM OX063 in H ₂ O/ethanol (2/1, v/v)

Table 3: Calculated OX063 Concentrations. Maximum and minimum values correspond to 0% and 100% water retention in the nanodroplets, respectively.

	Sample	A	B	C	D
OX063 concentration	min (mM)	3.5	9.7	9.7	9.8
	max (mM)	17.8	49.4	49.4	29.0

CFFGS Device

The CFFGS device was fabricated by electron-beam lithography and reactive ion-beam etching of a 100-nm thick Al film deposited on a sapphire substrate. The device contained a 150-nm

wide and 50-nm-long constriction, which served to focus electrical currents to produce the magnetic fields used for spin detection and control.

NMR and ESR Electronics

We used two arbitrary waveform generators (AWGs) to generate the spin control and detection waveforms applied to the CFFGS. One AWG was used to generate the MAGGIC waveforms at the SiNW frequency for spin detection, while the other generated NMR and ESR waveforms on separate channels. The ESR pulses were mixed in software with a 374 MHz carrier and then up-converted to 9.26 GHz using an IQ mixer. The signals were combined at the final stage using a diplexer and bias tees. To avoid spurious electron relaxation, we minimized electronic noise near 9.26 GHz by adding a fast switch to the output of the microwave amplifier, which provided a connection to the CFFGS only during application of the microwave pulses. A schematic of the electronics is provided in the Supplementary Materials.

Force-Detected Magnetic Resonance Microscope

Experiments were conducted under high vacuum using a custom-built force microscope operating in high vacuum at 4.2 K. Relative positioning between the SiNW chip, CFFGS and the optical fiber used for detecting the interferometric displacement of the SiNW was performed using a combination of nanopositioners and piezoelectric scanners.

References

1. C. L. Degen, M. Poggio, H. J. Mamin, C. T. Rettner, D. Rugar, *Nanoscale Magnetic Resonance Imaging*. *Proc. Natl. Acad. Sci. U.S.A* **106**, 1313 (2009).

2. J. M. Nichol, E. R. Hemesath, L. J. Lauhon, R. Budakian, *Nanomechanical Detection of Nuclear Magnetic Resonance using a Silicon Nanowire Oscillator*. *Phys. Rev. B* **85**, 054414 (2012).
3. P. Maletinsky, S. Hong, M. S. Grinolds, B. Hausmann, M. D. Lukin, R. L. Walsworth, M. Loncar, A. Yacoby, *A Robust Scanning Diamond Sensor for Nanoscale Imaging with Single Nitrogen-Vacancy Centres*. *Nat. Nanotechnol.* **7**, 320-324 (2012).
4. J. M. Nichol, T. R. Naibert, E. R. Hemesath, L. J. Lauhon, R. Budakian, *Nanoscale Fourier-Transform Magnetic Resonance Imaging*. *Phys. Rev. X* **3**, 031016 (2013).
5. T. Häberle, D. Schmid-Lorch, F. Reinhard, J. Wrachtrup, *Nanoscale Nuclear Magnetic Imaging with Chemical Contrast*. *Nat. Nanotechnol.* **10**, 125-128 (2015).
6. M. Kost, J. Cai, M. B. Plenio, *Resolving Single Molecule Structures with Nitrogen-Vacancy Centers in Diamond*. *Sci. Rep.* **5**, 11007 (2015).
7. A. Ajoy, U. Bissbort, M. D. Lukin, R. L. Walsworth, P. Cappellaro, *Atomic-Scale Nuclear Spin Imaging Using Quantum-Assisted Sensors in Diamond*. *Phys. Rev. X* **5**, 011001 (2015).
8. D. Rugar, H. J. Mamin, M. H. Sherwood, M. Kim, C. T. Rettner, K. Ohno, D. D. Awschalom, *Proton Magnetic Resonance Imaging using a Nitrogen–Vacancy Spin Sensor*. *Nat. Nanotechnol.* **10**, 120-124 (2015).
9. P. Wang, S. Chen, M. Guo, S. Peng, M. Wang, M. Chen, W. Ma, R. Zhang, J. Su, X. Rong, F. Shi, T. Xu, J. Du, *Nanoscale Magnetic Imaging of Ferritins in a Single Cell*. *Sci. Adv.* **5**, eaau8038 (2019).

10. W. Rose, H. Haas, A. Q. Chen, N. Jeon, L. J. Lauhon, D. G. Cory, R. Budakian, *High-Resolution Nanoscale Solid-State Nuclear Magnetic Resonance Spectroscopy. Phys. Rev. X* **8**, 011030 (2018).
11. M. H. Abobeih, J. Randall, C. E. Bradley, H. P. Bartling, M. A. Bakker, M. J. Degen, M. Markham, D. J. Twitchen, T. H. Taminiau, *Atomic-Scale Imaging of a 27-Nuclear-Spin Cluster using a Quantum Sensor. Nature* **576**, 411-415 (2019).
12. U. Grob, M. D. Krass, M. Héritier, R. Pachlatko, J. Rhensius, J. Košata, B. A. Moores, H. Takahashi, A. Eichler, C. L. Degen, *Magnetic Resonance Force Microscopy with a One-Dimensional Resolution of 0.9 Nanometers. Nano Letters* **19**, 7935-7940 (2019).
13. H. Haas, S. Tabatabaei, W. Rose, P. Sahafi, M. Piscitelli, A. Jordan, P. Priyadarsi, N. Singh, B. Yager, P. J. Poole, D. Dalacu, R. Budakian, *Nuclear Magnetic Resonance Diffraction with Subangstrom Precision. Proc. Natl. Acad. Sci. U.S.A* **119**, e2209213119 (2022).
14. M. Krass, N. Prumbaum, R. Pachlatko, U. Grob, H. Takahashi, Y. Yamauchi, C. L. Degen, A. Eichler, *Force-Detected Magnetic Resonance Imaging of Influenza Viruses in the Overcoupled Sensor Regime. Phys. Rev. Appl.* **18**, 034052 (2022).
15. Y. Tao, C. L. Degen, *Single-Crystal Diamond Nanowire Tips for Ultrasensitive Force Microscopy. Nano Lett.* **15**, 7893-7897 (2015).
16. M. Héritier, A. Eichler, Y. Pan, U. Grob, I. Shorubalko, M. D. Krass, Y. Tao, C. L. Degen, *Nanoladder Cantilevers Made from Diamond and Silicon. Nano Lett.* **18**, 1814-1818 (2018).
17. P. Sahafi, W. Rose, A. Jordan, B. Yager, M. Piscitelli, R. Budakian, *Ultralow Dissipation Patterned Silicon Nanowire Arrays for Scanning Probe Microscopy. Nano Lett.* **20**, 218-223 (2020).

18. Y. Tao, A. Eichler, T. Holzherr, C. L. Degen, *Ultrasensitive Mechanical Detection of Magnetic Moment using a Commercial Disk Drive Write Head*. *Nat. Commun.* **7**, 12714 (2016).
19. H. J. Mamin, C. T. Rettner, M. H. Sherwood, L. Gao, D. Rugar, *High Field-Gradient Dysprosium Tips for Magnetic Resonance Force Microscopy*. *Appl. Phys. Lett.* **100**, 013102 (2012).
20. S. Sangtawesin, B. L. Dwyer, S. Srinivasan, J. J. Allred, L. V. H. Rodgers, K. De Greve, A. Stacey, N. Dotschuk, K. M. O'Donnell, D. Hu, D. A. Evans, C. Jaye, D. A. Fischer, M. L. Markham, D. J. Twitchen, H. Park, M. D. Lukin, N. P. de Leon, *Origins of Diamond Surface Noise Probed by Correlating Single-Spin Measurements with Surface Spectroscopy*. *Phys. Rev. X* **9**, 031052 (2019).
21. M. Joos, D. Bluvstein, Y. Lyu, D. Weld, A. Bleszynski Jayich, *Protecting Qubit Coherence by Spectrally Engineered Driving of the Spin Environment*. *npj Quantum Inf.* **8**, 47 (2022).
22. W. Zheng, K. Bian, X. Chen, Y. Shen, S. Zhang, R. Stöhr, A. Denisenko, J. Wrachtrup, S. Yang, Y. Jiang, *Coherence Enhancement of Solid-State Qubits by Local Manipulation of the Electron Spin Bath*. *Nat. Phys.* **18**, 1317-1323 (2022).
23. J. H. Lee, Y. Okuno, S. Cavagnero, *Sensitivity Enhancement in Solution NMR: Emerging Ideas and New Frontiers*. *J. Magn. Reson.* **241**, 18-31 (2014).
24. J. Eills, D. Budker, S. Cavagnero, E. Y. Chekmenev, S. J. Elliott, S. Jannin, A. Lesage, J. Matysik, T. Meersmann, T. Prisner, J. A. Reimer, H. Yang, I. V. Koptyug, *Spin Hyperpolarization in Modern Magnetic Resonance*. *Chem. Rev.* **123**, 1417-1551 (2023).
25. A. S. Lilly Thankamony, J. J. Wittmann, M. Kaushik, B. Corzilius, *Dynamic Nuclear Polarization for Sensitivity Enhancement in Modern Solid-State NMR*. *Prog. Nucl. Magn. Reson. Spectrosc.* **102-103**, 120-195 (2017).

26. T. Can, Q. Ni, R. Griffin, *Mechanisms of Dynamic Nuclear Polarization in Insulating Solids. J. Magn. Reson.* **253**, 23-35 (2015).

27. R. Gupta, M. Lu, G. Hou, M. A. Caporini, M. Rosay, W. Maas, J. Struppe, C. Suiter, J. Ahn, I. L. Byeon, W. T. Franks, M. Orwick-Rydmark, A. Bertarello, H. Oschkinat, A. Lesage, G. Pintacuda, A. M. Gronenborn, T. Polenova, *Dynamic Nuclear Polarization Enhanced MAS NMR Spectroscopy for Structural Analysis of HIV-1 Protein Assemblies. J. Phys. Chem. B* **120**, 329-339 (2016).

28. A. Lesage, M. Lelli, D. Gajan, M. A. Caporini, V. Vitzthum, P. Miéville, J. Alauzun, A. Roussey, C. Thieuleux, A. Mehdi, G. Bodenhausen, C. Coperet, L. Emsley, *Surface Enhanced NMR Spectroscopy by Dynamic Nuclear Polarization. J. Am. Chem. Soc.* **132**, 15459-15461 (2010).

29. A. J. Rossini, C. M. Widdifield, A. Zagdoun, M. Lelli, M. Schwarzwälder, C. Copéret, A. Lesage, L. Emsley, *Dynamic Nuclear Polarization Enhanced NMR Spectroscopy for Pharmaceutical Formulations. J. Am. Chem. Soc.* **136**, 2324-2334 (2014).

30. P. Berruyer, M. Lelli, M. P. Conley, D. L. Silverio, C. M. Widdifield, G. Siddiqi, D. Gajan, A. Lesage, C. Copéret, L. Emsley, *Three-Dimensional Structure Determination of Surface Sites. J. Am. Chem. Soc.* **139**, 849-855 (2017).

31. K. Golman, J. H. Ardenkjær-Larsen, J. S. Petersson, S. Måansson, I. Leunbach, *Molecular Imaging with Endogenous Substances. Proc. Natl. Acad. Sci. U.S.A* **100**, 10435-10439 (2003).

32. M. C. Krishna, S. English, K. Yamada, J. Yoo, R. Murugesan, N. Devasahayam, J. A. Cook, K. Golman, J. H. Ardenkjær-Larsen, S. Subramanian, J. B. Mitchell, *Overhauser Enhanced Magnetic Resonance Imaging for Tumor Oximetry: Coregistration of Tumor*

Anatomy and Tissue Oxygen Concentration. Proc. Natl. Acad. Sci. U.S.A **99**, 2216-2221 (2002).

33. Y. Lee, G. S. Heo, H. Zeng, K. L. Wooley, C. Hilty, *Detection of Living Anionic Species in Polymerization Reactions Using Hyperpolarized NMR. J. Am. Chem. Soc* **135**, 4636-4639 (2013).
34. X. Ji, A. Bornet, B. Vuichoud, J. Milani, D. Gajan, A. J. Rossini, L. Emsley, G. Bodenhausen, S. Jannin, *Transportable Hyperpolarized Metabolites. Nat. Commun.* **8**, 13975 (2017).
35. H. Chen, M. Ragavan, C. Hilty, *Protein Folding Studied by Dissolution Dynamic Nuclear Polarization. Angew. Chem. Int. Ed.* **52**, 9192-9195 (2013).
36. S. J. Nelson, J. Kurhanewicz, D. B. Vigneron, P. E. Z. Larson, A. L. Harzstark, M. Ferrone, M. van Criekinge, J. W. Chang, R. Bok, I. Park, G. Reed, L. Carvajal, E. J. Small, P. Munster, V. K. Weinberg, J. H. Ardenkjaer-Larsen, A. P. Chen, R. E. Hurd, L. Odegardstuen, F. J. Robb, J. Tropp, J. A. Murray, *Metabolic Imaging of Patients with Prostate Cancer Using Hyperpolarized [1-13C] Pyruvate. Sci. Transl. Med.* **5**, 198ra108-198ra108 (2013).
37. H. J. Mamin, R. Budakian, B. W. Chui, D. Rugar, *Detection and Manipulation of Statistical Polarization in Small Spin Ensembles. Phys. Rev. Lett.* **91**, 207604 (2003).
38. B. E. Herzog, D. Cadeddu, F. Xue, P. Peddibhotla, M. Poggio, *Boundary Between the Thermal and Statistical Polarization Regimes in a Nuclear Spin Ensemble. Appl. Phys. Lett.* **105**, 043112 (2014).
39. N. Staudenmaier, A. Vijayakumar-Sreeja, G. Genov, D. Cohen, C. Findler, J. Lang, A. Retzker, F. Jelezko, S. Oviedo-Casado, *Optimal Sensing Protocol for Statistically Polarized Nano-NMR with NV Centers. Phys. Rev. Lett.* **131**, 150801 (2023).

40. L. Lumata, Z. Kovacs, A. D. Sherry, C. Malloy, S. Hill, J. van Tol, L. Yu, L. Song, M. E. Merritt, *Electron Spin Resonance Studies of Trityl OX063 at a Concentration Optimal for DNP*. *Phys. Chem. Chem. Phys.* **15**, 9800-9807 (2013).

41. T. V. Can, R. T. Weber, J. J. Walish, T. M. Swager, R. G. Griffin, *Ramped-amplitude NOVEL*. *J. Chem. Phys.* **146**, 154204 (2017).

42. B. Corzilius, *High-Field Dynamic Nuclear Polarization*. *Annu. Rev. Phys. Chem.* **71**, 143-170 (2020).

43. G. Mathies, S. Jain, M. Reese, R. G. Griffin, *Pulsed Dynamic Nuclear Polarization with Trityl Radicals*. *J. Phys. Chem. Lett.* **7**, 111-116 (2016).

44. C. E. Issac, C. M. Gleave, P. T. Nasr, H. L. Nguyen, E. A. Curley, J. L. Yoder, E. W. Moore, L. Chen, J. A. Marohn, *Dynamic Nuclear Polarization in a Magnetic Resonance Force Microscope Experiment*. *Phys. Chem. Chem. Phys.* **18**, 8806-8819 (2016).

45. H. Chen, A. G. Maryasov, O. Y. Rogozhnikova, D. V. Trukhin, V. M. Tormyshev, M. K. Bowman, *Electron Spin Dynamics and Spin-Lattice Relaxation of Trityl Radicals in Frozen Solutions*. *Phys. Chem. Chem. Phys.* **18**, 24954-24965 (2016).

46. S. Kolkowitz, A. Safira, A. A. High, R. C. Devlin, S. Choi, Q. P. Unterreithmeier, D. Patterson, A. S. Zibrov, V. E. Manucharyan, H. Park, M. D. Lukin, *Probing Johnson Noise and Ballistic Transport in Normal Metals with a Single-Spin Qubit*. *Science* **347**, 1129-1132 (2015).

47. R. P. Wang, *Defects in Silicon Nanowires*. *Appl. Phys. Lett.* **88**, 142104 (2006).

48. A. Baumer, M. Stutzmann, M. S. Brandt, F. C. Au, S. T. Lee, *Paramagnetic Defects of Silicon Nanowires*. *Appl. Phys. Lett.* **85**, 943-945 (2004).

49. K. L. Brower, T. J. Headley, *Dipolar Interactions Between Dangling Bonds at the (111) Si-SiO₂ Interface*. *Phys. Rev. B* **34**, 3610–3619 (1986).
50. B. Nouwen, A. Stesmans, *Dependence of Strain at the (111) Si/SiO₂ Interface on Interfacial Si Dangling-Bond Concentration*. *Mater. Sci. Eng., A* **288**, 239-243 (2000).
51. R. Rurali, *Colloquium: Structural, Electronic, and Transport Properties of Silicon Nanowires*. *Rev. Mod. Phys.* **82**, 427–449 (2010).
52. A. Stesmans, *The .Si Identical to Si₃ Defect at Various (111)Si/SiO₂ and (111) Si/Si₃N₄ Interfaces*. *Semicond. Sci. Technol.* **4**, 1000 (1989).
53. N. Bloembergen, *On the Interaction of Nuclear Spins in a Crystalline Lattice*. *Physica* **15**, 386-426 (1949).
54. A. E. Dementyev, D. G. Cory, C. Ramanathan, *Dynamic Nuclear Polarization in Silicon Microparticles*. *Phys. Rev. Lett.* **100**, 127601 (2008).
55. M. Poggio, C. L. Degen, H. J. Mamin, D. Rugar, *Feedback Cooling of a Cantilever's Fundamental Mode below 5 mK*. *Phys. Rev. Lett.* **99**, 017201 (2007).

Acknowledgements: The University of Waterloo's QNFCF facility was used for this work. This infrastructure would not be possible without the significant contributions of CFREF-TQT, CFI, Industry Canada, the Ontario Ministry of Research and Innovation and Mike and Ophelia Lazaridis. Their support is gratefully acknowledged. We would like to thank D. Akhmetzyanov and T. W. Borneman for helpful discussions and D. G. Cory for providing the trityl-OX063 samples, and useful comments.

Funding: This work was undertaken thanks in part to funding from the Canada First Research Excellence Fund (CFREF), and the Natural Sciences and Engineering Research Council of

Canada (NSERC).

Author Contributions: Conceptualization: R.B. Measurements and data analysis: S.T., P.P. and N.S. Simulations: N.S., D.T., P.P. and S.T. SiNW growth: P.S. and A.J. Sample preparation: P.P. Writing (original draft): S.T. and R.B. Writing (review and edits): S.T., P.P., N.S, D.T. and R.B. Supervision: R.B. Resources: R.B.

Competing Interests: The authors declare that they have no competing financial interests.

Data and materials availability: All data needed to evaluate the conclusions in the paper are present in the paper and/or the Supplementary Materials.

Supplementary Materials for Large-Enhancement Nanoscale Dynamic Nuclear Polarization Near a Silicon Nanowire Surface

Sahand Tabatabaei,^{1,2} Pritam Priyadarsi,^{1,2} Namanish Singh,^{1,2}
Pardis Sahafi,^{1,2} Daniel Tay,^{1,2} Andrew Jordan,^{1,2} Raffi Budakian^{1,2*}

¹Department of Physics and Astronomy, University of Waterloo, Waterloo, ON, Canada, N2L3G1

²Institute for Quantum Computing, University of Waterloo, Waterloo, ON, Canada, N2L3G1

*To whom correspondence should be addressed; E-mail: rbudakian@uwaterloo.ca.

1 Sample Preparation and Attachment

1.1 Silicon Nanowire Etching

Before attaching the OX063 samples to the silicon nanowire (SiNW), the Au ball at the nanowire's tip was etched to mitigate potential charge interactions with the CFFGS. An iodine-based etchant, comprising 207 mg KI and 54 mg I₂ in 1.43 mL of DI H₂O and 0.36 mL Ethanol, was prepared. Ethanol was added to reduce the surface tension of the solution, a requirement in the subsequent Au etching and sample attachment steps.

A G-1 Narishige glass capillary is pulled into a pipette using the Narishige PC-10 pipette puller. The pipette tip is ground on a Narishige EG-402 micro-grinder until an orifice of approximately 20 μ m in diameter is obtained. This pipette is affixed to one arm of the MMO-203 micro-manipulator which is, in turn, connected to the Narishige IM-11-2 pneumatic microinjector. A few drops of the etchant solution were drawn into the pipette. The SiNW and the

capillary tip were aligned under an optical microscope. The etchant was pushed out through the orifice until a curvature was seen. The capillary, guided by the micromanipulator, was moved towards the SiNW and brought in contact with its tip. The reduction in surface tension enabled by the Ethanol allowed for the SiNW tip to penetrate the etchant droplet. This configuration is maintained for up to 2 minutes for complete Au etching. Subsequently, the SiNW tip is cleaned with a 1:1 DI H₂O and Ethanol solution using the micromanipulator and a new glass capillary.

1.2 Sample Solution Preparation

To prepare the various OX063 samples, stock solutions with different amounts of constituents were prepared. Table S1 summarizes the constituents for each of the samples.

Table S1: **Constituent table**, including all the components used to prepare the measured samples.

Constituents	A	B	C	D
Sucrose (mg); C ₁₂ H ₂₂ O ₁₁	-	-	-	80.7
Glucose (mg); C ₆ H ₁₂ O ₆	6.0	6.1	6.1	-
d-12 Glucose (mg); C ₆ D ₁₂ O ₆	54.0	54.4	54.4	-
H ₂ O (μL)	15	15	15	100
D ₂ O (μL)	135	135	135	-
Ethanol (μL)	-	-	-	50
d-Ethanol (μL)	150	150	150	-
OX063 (mg)	0.92	2.58	2.58	2.10
Concentration (mM)	17.8	49.4	49.4	29

The mixing process began with adding the sugar and the OX063 radicals in the amount given in Table S1 into a 4 mL amber glass vial. Micro-pipettes were then used to pipette the appropriate amount of water into the vial with the sugar and radical mixture. This vial was then pushed onto a vortex shaker to dissolve the sugar and the radicals. Once the dissolution was complete, the appropriate amount of ethanol was pipetted into the mixture, followed by another round on the vortex shaker.

The constituents of the deuterated samples were chosen to ensure a 9:1 ratio of proton to deuterium in the sample (assuming complete evaporation of Ethanol). These ratios were finalized in an attempt to match the concentration ratio of proton to deuterium in DNP juice (1).

1.3 Sample Attachment

Once the Au etching and cleaning process is completed, the sample is attached to the SiNW tip as follows. The sample solution is drawn into a pointed-tip glass capillary and aligned in front of a SiNW under an optical microscope. Prior to attachment, dry N₂ gas is blown over the 20 μ m diameter orifice of the capillary. The nitrogen flow creates a higher concentration of sugar on the surface of the droplet exiting the capillary, which facilitates the formation of the nano-droplet on the tip of the SiNW. Without the N₂ flow, the sample failed to remain attached to the SiNW as the capillary was pulled back.

2 CFFGS Fabrication and Field Profile

2.1 CFFGS Fabrication

The current-focusing field gradient source (CFFGS) is a lithographically fabricated nanoscale metallic constriction that generates the magnetic field gradients used for spin detection and the magnetic fields used for spin control. Fig. S1A shows an optical image of the CFFGS. The image was constructed by combining multiple optical images and refining them with image editing software. The device is a microstrip transmission line engineered to operate in the X-band. Finite element method simulations using HFSS indicated an insertion loss of 0.7 dB at 9.26 GHz for the device.

The device is fabricated by UHV sputtering a 100 nm thick Al film on a sapphire substrate. The head section of the device, shown in Fig. S1B, is patterned via e-beam lithography and metal reactive ion etching. The remaining section of the leads is thickened to 400 nm by de-

positing an additional Al layer to lower the device's electrical resistance. An SEM image of the thickened layer is shown in Fig. S1C. Lastly, the ground plane of the microstrip is made by depositing a 100 nm thick Al layer on the back side of the sapphire wafer.

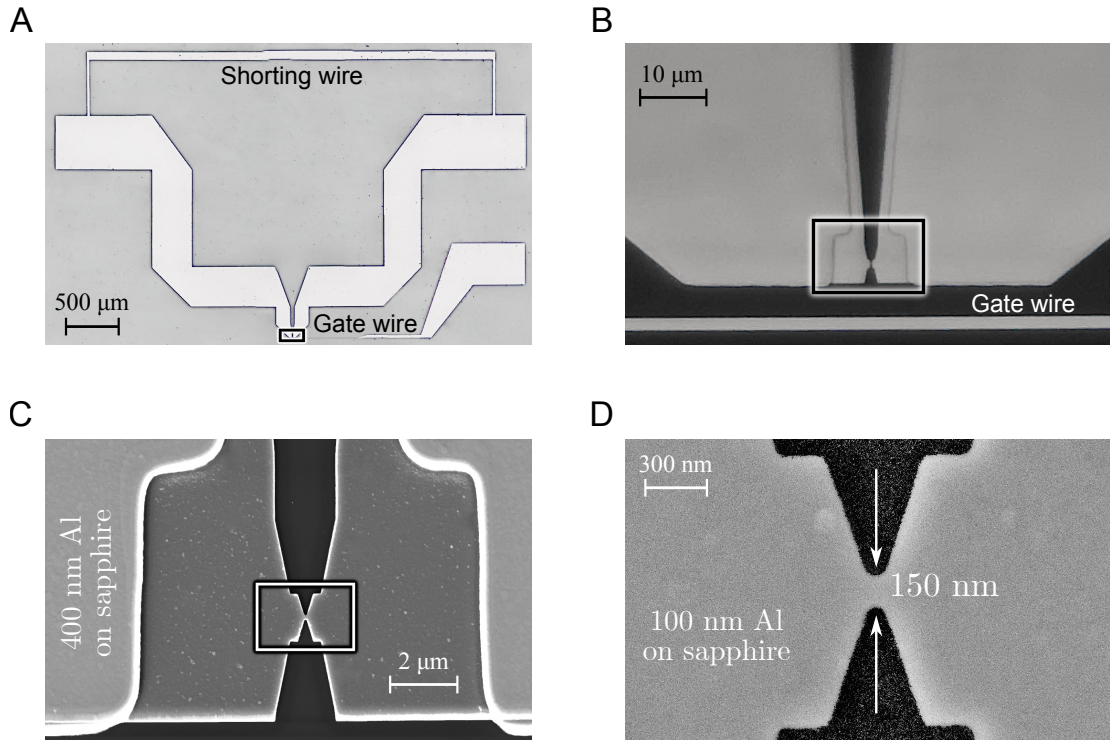


Figure S1: CFFGS Images. **(A)** Optical image of the CFFGS. **(B)** Optical image of the head section of the CFFGS. The metal lead on the lower part of the figure is connected to the gate shown in **(A)** used to apply an electrostatic potential to the SiNW. **(C)** SEM of the constriction section of the CFFGS. **(D)** SEM of the constriction.

The shorting wire, seen on the top section of Fig. S1A, is fabricated to prevent electrostatic discharge through constriction during the fabrication processes. The connection is broken by scribing the wire after wire bonding the leads to the PCB carrier. The gate, seen in the lower part of Fig. S1B, is used to mitigate interactions between the CFFGS and charges on the surface of the sample by applying a voltage bias.

2.2 Field Profiles

The magnetic field configuration produced by the CFFGS is calculated using the COMSOL finite element simulation software. The simulated Rabi field $B_1(\mathbf{r}) = \sqrt{B_x^2(\mathbf{r}) + B_y^2(\mathbf{r})}/2$ and the detection gradient $G(\mathbf{r}) = \partial B_y(\mathbf{r})/\partial z$ are shown in Fig. S2.

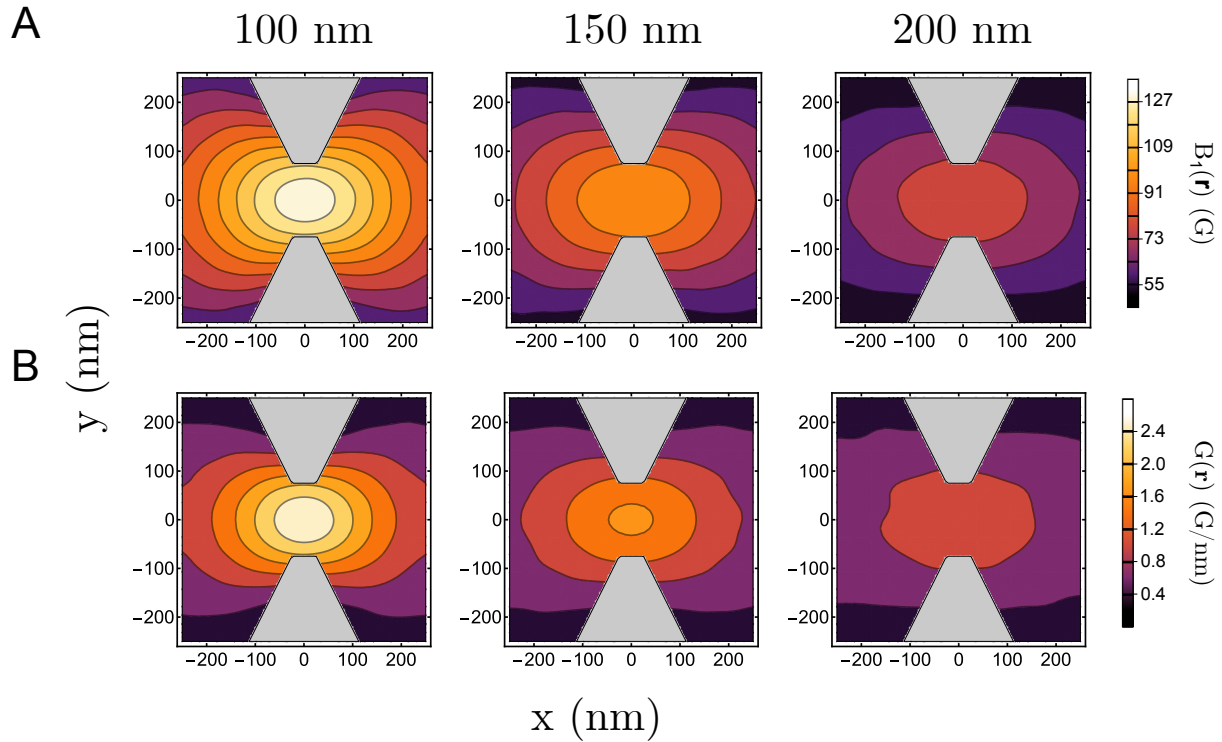


Figure S2: **CFFGS Field Distribution.** **(A)** Simulated Rabi field contours and **(B)** Simulated detection gradient contours at different heights above the center of the CFFGS. The B_1 profiles were generated for a peak current of 29 mA while the $G(\mathbf{r})$ profiles were generated for a peak current of 47 mA passing through the CFFGS.

3 MAGGIC protocol

Here, we briefly discuss the MAGGIC spin detection protocol, while referring to (2, 3) for a detailed description. The modulated alternating gradients generated with currents (MAGGIC) protocol, depicted in Fig. S3, converts the z -axis spin magnetization to a resonant force on the

SiNW oscillator. After implementing the spin control sequence of interest e.g., the imaging sequence shown in Fig. 5A in the main text, a measurement block with a duration of τ_0 is applied. The measurement involves the repeated application of the MAGGIC waveform primitive (Fig. S3A), in which we modulate the $G(\mathbf{r}) = \partial B_z(\mathbf{r})/\partial y$ gradient at the SiNW resonance frequency ω_c by driving a current $I_c(t)$ through the CFFGS. The gradient modulation is phase shifted by π between successive MAGGIC waveform primitives to avoid spurious electrical forces at ω_c . The polarization of the spins being measured is inverted between two MAGGIC primitives using an adiabatic full passage (AFP), which combined with the phase shift of the gradient modulation, results in a resonant force

$$\mathcal{F}(t) = \frac{\mu D}{\sqrt{2}} \int d^3r n(\mathbf{r})G(\mathbf{r})h(\mathbf{r}, t) + \mathcal{N}(t) \quad (\text{S1})$$

at ω_c . Here, $D = \tau_1/(\tau_1 + \tau_2)$ is the duty cycle of the gradient modulation (Fig. S3A), μ is the spin magnetic moment, $n(\mathbf{r})$ is the spin density at position \mathbf{r} , and $\mathcal{N}(t)$ is the oscillator's thermal force noise, which is a stationary white random process. $h(\mathbf{r}, t) \in \{-1, 1\}$ is a random telegraph process that models the random evolution of the z projection of the spin during the measurement (3). The number of sign flips of h over a given time interval is Poisson distributed, which results in the autocorrelation $\langle h(\mathbf{r}, t_1)h(\mathbf{r}, t_2) \rangle = e^{-|t_2 - t_1|/\tau_m}$. The spin correlation time τ_m encompasses the combined effect of the AFP infidelity and T_1 relaxation during the MAGGIC protocol.

For the enhancement measurements presented in Fig. 4 of the main text, $D = 72.3\%$ ($\tau_1 = 42.28 \mu\text{s}$, $\tau_2 = 16.17 \mu\text{s}$), and the measure block duration was $\tau_0 = 200 \text{ ms}$. For the imaging experiments presented in Fig. 5 of the main text, the duty cycle was increased to $D = 90.2\%$ ($\tau_1 = 154.4 \mu\text{s}$, $\tau_2 = 16.78 \mu\text{s}$) to improve the SNR. The measure block duration was also increased to $\tau_0 = 400 \text{ ms}$ to accommodate the larger τ_m achieved via electron decoupling (Fig. 5 of the main text). The AFP used in the MAGGIC waveform was the numerically-optimized 2.3

Rabi-cycle AFP presented in Ref. (4). The AFP was $15.44\ \mu\text{s}$ long and inverts proton spins with Rabi frequencies $\omega_{1I}/(2\pi) \geq 150\ \text{kHz}$.

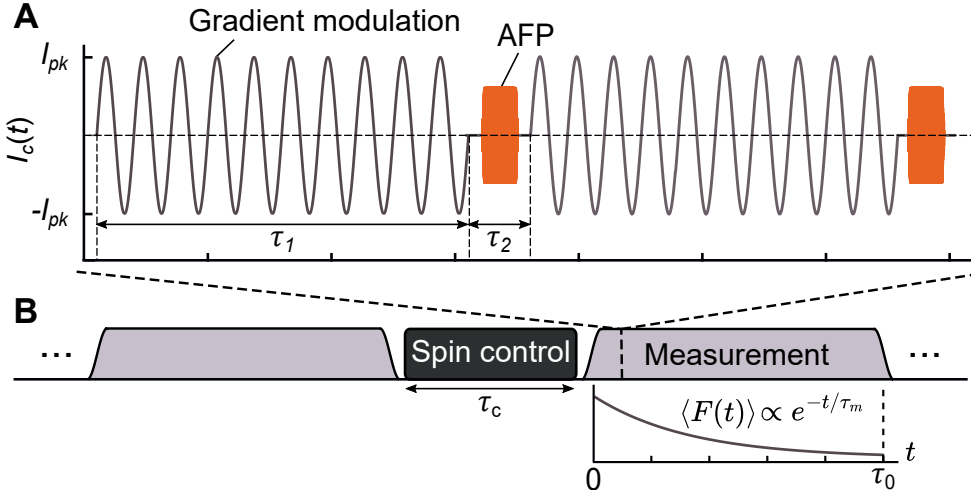


Figure S3: **General Schematic of the MAGGIC Protocol.** (A) The MAGGIC waveform primitive. (B) A typical nanoscale magnetic resonance experiment, including the spin control and measurement blocks. The spin control block contains the spin control pulses of interest, e.g. imaging pulses, DNP, etc. The MAGGIC waveform generates a resonant force on the spins, which decays exponentially (bottom figure).

3.1 Average Polarization Measurements

For measurements using the average polarization, we measure the sample average $F(t) = \sum_{k=1}^M \mathcal{F}_i(t)/M$ over M realizations of the force from Eq. S1, where the index i denotes the i^{th} realization. Each spin builds up an average polarization $m_0(\mathbf{r}) = \langle h(\mathbf{r}, 0) \rangle$ at the start of a measurement block. The associated probability distribution is $\mathbb{P}[h(\mathbf{r}, 0) = \pm 1] = (1 \pm m_0(\mathbf{r})) / 2$. This, along with the Poisson distribution governing the number of spin flips, determines $\langle h(\mathbf{r}, t) \rangle = m_0(\mathbf{r})e^{-t/\tau_m}$, which results in an expectation value of the force signal equal to

$$\langle F(t) \rangle = \frac{\mu D}{\sqrt{2}} e^{-t/\tau_m} \int d^3r n(\mathbf{r}) G(\mathbf{r}) m_0(\mathbf{r}). \quad (\text{S2})$$

This exponentially decaying force resonant with the SiNW translates to a mean displacement

$$\langle Y(t) \rangle = \frac{\mu D Q_c}{\sqrt{2}k} \frac{e^{-t/\tau_m} - e^{-t/\tau_Q}}{1 - \tau_Q/\tau_m} \int d^3r n(\mathbf{r}) G(\mathbf{r}) m_0(\mathbf{r}), \quad (\text{S3})$$

which is detected with optical interferometry. Here, k is the spring constant, $Q_c \sim 900$ is the damped quality factor, and $\tau_Q = 2Q_c/\omega_c \sim 1$ ms is the characteristic response time of the oscillator. Since $\tau_m \gg \tau_Q$, we have $\langle Y(t) \rangle \simeq (Q_c/k)\langle F(t) \rangle$ for $t \gg \tau_Q$, i.e. the measured displacement is proportional to the force, apart from the fast initial rise in the signal due to the oscillator's finite bandwidth. Eq. S3 is the model used for the fits in Fig 4B of the main text.

We process the acquired force record $F(t)$ using a matched filtering scheme for optimal SNR (5). Assuming the noise in the measured $F(t)$ is approximately white, we seek a kernel $w(t)$, for which the inner product $\bar{F} = \langle w|F \rangle = \int_0^{\tau_0} dt w(t) F(t)$ maximizes the SNR = $\langle \bar{F} \rangle / \sqrt{\text{Var}(\bar{F})} \propto \langle w|F \rangle / \|w\|$. Here, $\text{Var}(\bar{F})$ denotes the variance of \bar{F} . By the Cauchy-Schwartz inequality, the optimal kernel is $w(t) \propto F(t)$. Therefore, we fit a function of the form Eq. S3 to the measured hyperpolarized $F(t)$ of each sample, and use it for $w(t)$. We then normalize $w(t)$ such that $\int_0^{\tau_0} dt w(t) = 1$ to ensure that \bar{F} can be interpreted as a weighted average of $F(t)$. Since $\tau_Q \ll \tau_0, \tau_m$, we can neglect the fast initial rise in Eq. S3, and approximately take $w(t) \propto e^{-t/\tau_m}$. This, along with Eq. S2 gives the average matched-filter output

$$\langle \bar{F} \rangle = \frac{\mu D}{2\sqrt{2}} (1 + e^{-\tau_0/\tau_m}) \int d^3r n(\mathbf{r}) G(\mathbf{r}) m_0(\mathbf{r}). \quad (\text{S4})$$

For a calculation of the fluctuations around this mean value, and the corresponding detection SNR, see Section 4.

3.2 Statistical Polarization Measurements

For measurements using statistical polarization, we construct a correlation function between the time-averaged $\mathcal{F}(t)$ force signal between adjacent measurement blocks:

$$C = \frac{1}{M-1} \sum_{i=1}^{M-1} \bar{F}_i \bar{F}_{i+1}, \quad (\text{S5})$$

where \bar{F}_i is the time-average of \mathcal{F} over the i^{th} measurement block. For statistical polarization measurements, \bar{F}_i is calculated with uniform weighting, i.e. $w(t) = 1/\tau_0$. The average correlation $\langle C \rangle$ is (2, 3)

$$\langle C \rangle = \frac{\mu^2 D^2}{2} e^{-\tau_c/\tau_m} \left(\frac{\tau_m}{\tau_0} \right)^2 \left(1 - e^{-\tau_0/\tau_m} \right)^2 \int d^3r n(\mathbf{r}) G^2(\mathbf{r}) \zeta(\mathbf{r}), \quad (\text{S6})$$

where τ_c is the duration of the spin control block, and $\zeta(\mathbf{r}) = \text{Tr}[\sigma_z \varrho_f(\mathbf{r})]$ is the proportional to the expectation value of the z component of the spin, and $\varrho_f(\mathbf{r})$ is the reduced density matrix of a spin at position \mathbf{r} , which is the result of evolution under the spin control block starting from the $|\uparrow\rangle$ state. For a calculation of the fluctuations in the measured correlation C , and the corresponding detection SNR, see Section 4.

Importantly, comparing Eq. S6 to Eq. S4 shows that the signal contribution from each spin is weighted by the square of the detection gradient $G^2(\mathbf{r})$ for statistical polarization measurements, whereas average polarization measurements have a $G(\mathbf{r})$ weighting. Therefore, the effective detection volume for statistical measurements is smaller, and more confined to near the CFFGS surface. Fig. S4 illustrates this by showing the simulated spatial distribution of the hyperpolarized and statistical signals using the geometry of sample A, and the simulated CFFGS field gradients given in Section 2.2.

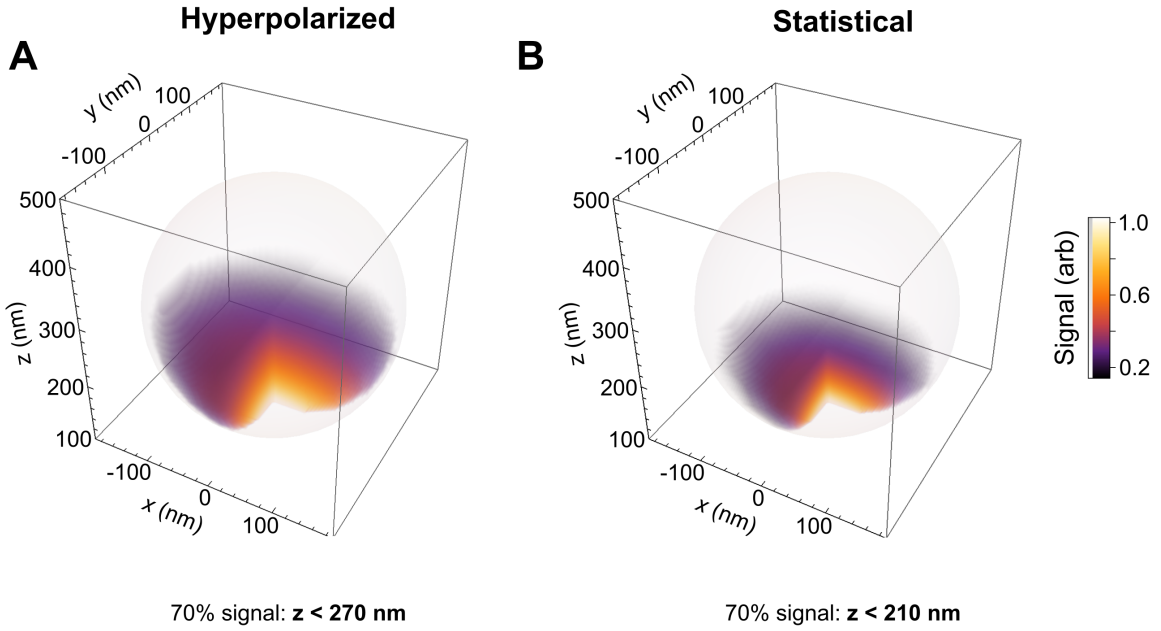


Figure S4: Effective Detection Volume for Statistical and Hyperpolarized Measurements. Simulated spatial distribution of the proton signal for the Sample A geometry using (A) hyperpolarized and (B) statistical polarization measurements. The signal is more confined to the tip for the statistical measurement due to the $G^2(\mathbf{r})$ weighting in the correlation signal (Eq. S6). The volume corresponding to 70% of the full signal is $(240 \text{ nm})^3$ and $(195 \text{ nm})^3$ for the hyperpolarized and statistical signals, respectively. The total volume of the sample is $(301 \text{ nm})^3$.

4 Theoretical SNR Comparison of Statistical and Average Polarization Measurements

In this section, we provide a detailed theoretical comparison of the SNR for measuring the average and statistical polarization using the MAGGIC protocol. The dominant sources of noise in force-detected nanoMRI platforms are 1) thermal force noise from the nanomechanical oscillator, and 2) random fluctuations of the spin polarization, i.e. spin noise. In the following, we calculate the variance of the average spin force \bar{F} and spin correlation C due to these two noise sources.

Average Polarization Measurements

Assuming statistically independent acquisitions, $\text{Var}(\bar{F})$ is calculated using Eq. S1

$$\begin{aligned}\text{Var}(\bar{F}) &= \text{Var} \left(\frac{1}{M} \sum_{i=1}^M \int_0^{\tau_0} dt w(t) \mathcal{F}_i(t) \right) \\ &= \frac{\mu^2 D^2}{2M} \int d^3r n(\mathbf{r}) G^2(\mathbf{r}) \int_0^{\tau_0} dt_1 \int_0^{\tau_0} dt_2 w(t_1) w(t_2) \text{Cov}[h(\mathbf{r}, t_1), h(\mathbf{r}, t_2)] + \frac{S_F}{2M} \|w\|^2,\end{aligned}\quad (\text{S7})$$

where $h(\mathbf{r}, t)$ is assumed to be uncorrelated for the different spins, and $S_F = 4k_B kT/(\omega_c Q)$ is the single-sided power spectral density of the oscillator force noise $\mathcal{N}(t)$. Here, Q is the native (undamped) quality factor of the oscillator. Since $m_0(\mathbf{r}) \ll 1$, $\text{Cov}[h(\mathbf{r}, t_1), h(\mathbf{r}, t_2)] \approx \langle h(\mathbf{r}, t_1)h(\mathbf{r}, t_2) \rangle = e^{-|t_2-t_1|/\tau_m}$, which, along with $w(t) \propto e^{-t/\tau_m}$, results in

$$\text{Var}(\bar{F}) = \frac{\tau_0 + \tau_c}{T_e} \left[\frac{\mu^2 D^2}{4} \frac{(1 - e^{-2\tau_0/\tau_m}) - 2\frac{\tau_0}{\tau_m} e^{-\frac{2\tau_0}{\tau_m}}}{(1 - e^{-\tau_0/\tau_m})^2} \int d^3r n(\mathbf{r}) G^2(\mathbf{r}) + \frac{S_F}{4\tau_m} \frac{1 + e^{-\tau_0/\tau_m}}{1 - e^{-\tau_0/\tau_m}} \right], \quad (\text{S8})$$

with $T_e = M(\tau_0 + \tau_c)$ being the total experiment duration.

Statistical Polarization Measurements

To calculate the fluctuations in the correlation C from Eq. S5, we follow a method similar to Ref. (6). This is done in the absence of a spin control block, i.e. $\zeta(\mathbf{r}) = 1$. We write the time-averaged force signal of the i^{th} measurement block as $\bar{F}_i = \bar{f}_i + \bar{\mathcal{N}}_i$, where \bar{f}_i and $\bar{\mathcal{N}}_i$ denote the contributions of the spin and oscillator force noise, respectively. We thus have

$C = C_{ff} + C_{fn} + C_{nf} + C_{nn}$, where

$$\begin{aligned}C_{ff} &= \frac{1}{M-1} \sum_{i=1}^{M-1} \bar{f}_i \bar{f}_{i+1}, & C_{fn} &= \frac{1}{M-1} \sum_{i=1}^{M-1} \bar{f}_i \bar{\mathcal{N}}_{i+1}, \\ C_{nf} &= \frac{1}{M-1} \sum_{i=1}^{M-1} \bar{\mathcal{N}}_i \bar{f}_{i+1}, & C_{nn} &= \frac{1}{M-1} \sum_{i=1}^{M-1} \bar{\mathcal{N}}_i \bar{\mathcal{N}}_{i+1},\end{aligned}$$

It is straightforward to check that all four terms are pairwise uncorrelated. Hence, $\text{Var}(C) = \text{Var}(C_{ff}) + \text{Var}(C_{fn}) + \text{Var}(C_{nf}) + \text{Var}(C_{nn})$. The first and last terms capture fluctuations in the sample correlation due to spin noise and oscillator noise, respectively, while the other two terms encompass the covariance between the two. Each term is calculated using standard formulae for the variance of the sample autocovariance and cross-covariance functions in the $M \gg 1$ limit (7, 8). For the first term, this gives

$$\text{Var}(C_{ff}) = \frac{1}{M} A\left(\frac{\tau_0}{\tau_m}, \frac{\tau_c}{\tau_m}\right) \sigma_f^4, \quad (\text{S9})$$

where

$$\sigma_f^2 \equiv \text{Var}(\bar{f}_i) = \mu^2 D^2 \left(\frac{\tau_m}{\tau_0}\right) \left(1 - (1 - e^{-\tau_0/\tau_m}) \frac{\tau_m}{\tau_0}\right) \int d^3r n(\mathbf{r}) G^2(\mathbf{r}) \quad (\text{S10})$$

is the variance of the time-averaged spin signal, and A is the dimensionless function

$$A(u, v) \equiv 1 + \frac{(e^u - 1)^2}{4(e^{2(u+v)} - 1)(1 + (u-1)e^u)^2} \times \\ \left[2(e^u - 1)^2 + (e^u - 1)^2 (1 + e^{-2(u+v)}) + 4(1 + (u-1)e^u)(1 - e^{-2(u+v)}) \right]. \quad (\text{S11})$$

Similarly,

$$\text{Var}(C_{fn}) = \frac{\text{Var}(\bar{f}_i)\text{Var}(\bar{\mathcal{N}}_i)}{M} = \frac{S_F \sigma_f^2}{2M\tau_0}, \quad (\text{S12})$$

and

$$\text{Var}(C_{nn}) = \frac{\text{Var}(\bar{\mathcal{N}}_i)^2}{M} = \frac{S_F^2}{4\tau_0^2 M}. \quad (\text{S13})$$

Putting Eq. S9,S12,S13 together, and using the fact that $\text{Var}(C_{nf}) = \text{Var}(C_{fn})$ and $M = T_e/(\tau_0 + \tau_c)$, we finally get

$$\text{Var}(C) = \frac{\tau_c + \tau_0}{T_e} \left[A\left(\frac{\tau_0}{\tau_m}, \frac{\tau_c}{\tau_m}\right) \sigma_f^4 + \frac{S_F \sigma_f^2}{\tau_0} + \frac{S_F^2}{4\tau_0^2} \right]. \quad (\text{S14})$$

SNR Comparison

Using the above results, we can compare the detection SNR between hyperpolarized and statistical measurements of proton spins. In the hyperpolarized case, we calculate $\text{SNR}_{\text{hp}} = \langle \bar{F} \rangle / \sqrt{\text{Var}(\bar{F})}$ by combining Eq. S4,S8, assuming uniform proton density, and using the fact that $\tau_c = T_b \gg \tau_0 \gg \tau_m$. This gives

$$\text{SNR}_{\text{hp}} \approx \sqrt{\frac{T_e}{2T_b}} \frac{N\epsilon p_T \mu D \bar{G}}{\sqrt{N\mu^2 D^2 \bar{G}^2 + S_F/\tau_m}}, \quad (\text{S15})$$

where N is the number of proton spins, $p_T = \hbar\omega_{0I}/(2k_B T)$ is the proton thermal polarization, ϵ is the polarization enhancement, and \bar{G} and \bar{G}^2 are the average values of $G(\mathbf{r})$ and $G^2(\mathbf{r})$ over the sample volume, respectively.

In the case of statistical polarization measurements, the final expression for $\text{SNR}_{\text{st}} = \langle C \rangle / \sqrt{\text{Var}(C)}$ is rather complicated. To compare with the hyperpolarized case, we instead work with an upper bound for SNR_{st} , which we construct using the fact that $A(\tau_0/\tau_m, \tau_c/\tau_m)\sigma_f^4 + S_F\sigma_f^2/\tau_0 + S_F^2/(4\tau_0^2) \geq A(\tau_0/\tau_m, \tau_c/\tau_m)\sigma_f^4$. This, along with $\tau_c \ll \tau_0$, results in the bound

$$\text{SNR}_{\text{st}} \leq \frac{1}{2} \sqrt{\frac{T_e}{\tau_m}} \frac{(1 - e^{-\tau_0/\tau_m})^2}{\sqrt{\frac{\tau_0}{\tau_m} A\left(\frac{\tau_0}{\tau_m}, 0\right)} \left[\frac{\tau_0}{\tau_m} - 1 + e^{-\tau_0/\tau_m}\right]}, \quad (\text{S16})$$

The largest value the right hand side can take across different τ_0/τ_m is $\sqrt{2}$. This gives the final upper bound on the statistical SNR:

$$\text{SNR}_{\text{st}} \leq \sqrt{\frac{T_e}{2\tau_m}}. \quad (\text{S17})$$

Combining Eq. S15,S17 gives the sufficient condition $\epsilon > \epsilon_b$ for $\text{SNR}_{\text{hp}} > \text{SNR}_{\text{st}}$, where

$$\epsilon_b = \frac{1}{p_T} \sqrt{\frac{T_b}{\tau_m} \frac{1}{N} \left(\frac{\bar{G}^2}{\bar{G}} \right) + \frac{T_b S_F}{2\tau_m^2 N^2 \mu^2 \bar{G}^2}}, \quad (\text{S18})$$

where we also assumed $D \approx 1$. An enhancement larger than ϵ_b will guarantee a higher SNR when using DNP, irrespective of the details of the measurement protocol.

In Fig. S5B, we provide the calculated ϵ_b from Eq. S17 for the samples presented in this work, along with the utilized parameters. The average gradient \bar{G} and gradient squared \bar{G}^2 were calculated using the simulated CFFGS field distribution (Section 2.2), and S_F was estimated using the measured frequency, quality factor and spring constant for each SiNW. The number of protons was estimated using the calculated proton density and the sample volume. All other parameters are taken from Table 1 of the main text.

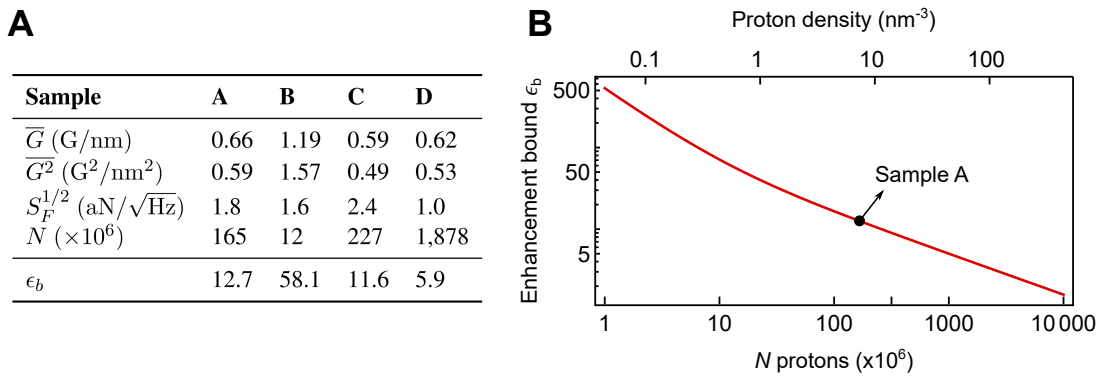


Figure S5: Calculated Lower Bound on the Polarization Enhancement ϵ_b . (A) Parameters used in the calculation, and the resulting ϵ_b for the different samples. (B) Calculated ϵ_b as a function number of protons, assuming the same parameters as sample A. The number of protons is varied by changing the spin density while the sample volume (and hence \bar{G} , \bar{G}^2) is held constant. A DNP enhancement above ϵ_b guarantees an SNR-advantage over measuring statistical polarization. The black dot in subfigure B corresponds to the calculated proton density for sample A, assuming no remaining water in the sugar droplet.

5 Spin Relaxation Measurements

The electron spin and proton spin relaxation times were characterized for all the samples used in the experiment. Here, we present the measured data for sample A, while referring to Table S2 for the other samples. These include the longitudinal and transverse relaxation times for protons T_{1p} , T_{2p}^* , T_{2p} , and electrons T_{1e} , T_{2e}^* , T_{1pe} . The relaxation curves and corresponding pulse sequences are shown in Fig. S6.

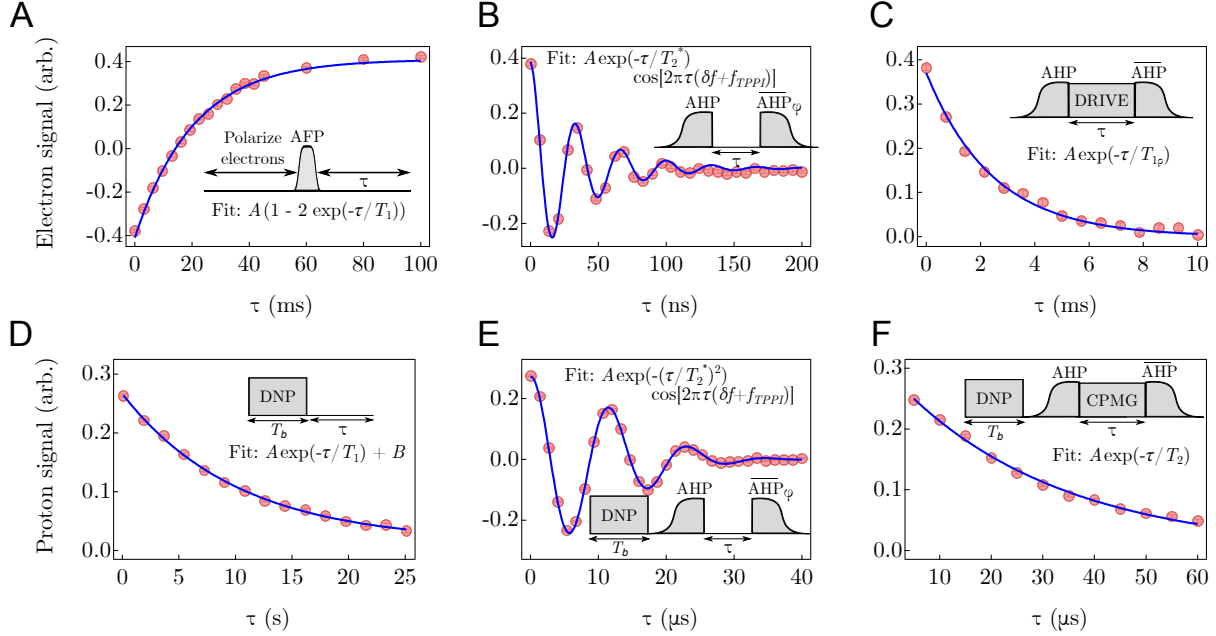


Figure S6: Relaxation Times. Spin relaxation data for sample A along with the pulse sequences used to perform the measurements. **(A)** Electron T_{1e} measurement with inversion recovery. **(B)** Electron T_{2e}^* measurement using a modified Ramsey experiment. To enhance sensitivity to the resonance offset, an artificial resonance offset of 30 MHz was introduced using a time-proportional phase increment (TPPI) scheme. **(C)** Electron T_{1pe} measurement with a resonant constant-amplitude drive. **(D)** Proton T_{1p} measurement by measuring the decay in the longitudinal magnetization of the hyperpolarized proton ensemble. **(E)** Proton T_{2p}^* measurement using a Ramsey experiment on the hyperpolarized proton ensemble with a TPPI frequency shift of 80 kHz. **(F)** Proton T_{2p} measurement with a σ_z decoupling sequence on the proton hyperpolarized ensemble.

T_{1e} was measured using an inversion recovery sequence, wherein the electrons were polarized, and inverted using an AFP. The spins were then allowed to equilibrate for a variable time τ , after which the longitudinal magnetization was measured (Fig. S6A). An exponential fit to the data gives $T_{1e} = 20.5(3)$ ms.

The electron T_{2e}^* was measured using a modified Ramsey experiment with a time-proportional phase-increment (TPPI) scheme. Here, the spins were tipped into the transverse plane using an AHP, followed by a variable free-evolution time τ . Subsequently, an inverse AHP with a phase

Table S2: **Electron and proton relaxation times** for all the measured samples. T_{2p} and T_{2p}^* were not measured for sample D.

	Relaxation Time	A	B	C	D
Electrons	T_{1e} (ms)	20.5(3)	2.5(1)	28.6(7)	30.0(4)
	T_{2e}^* (ns)	38(2)	27(3)	42(2)	50(3)
	$T_{1\rho e}$ (ms)	2.5(1)	0.45(4)	3.2(1)	7.5(3)
Protons	T_{1p} (s)	10.2(3)	1.01(3)	10.8(6)	20(1)
	T_{2p}^* (μ s)	17.0(2)	16.8(2)	16.8(2)	-
	T_{2p} (μ s)	31.4(7)	31(1)	30(1)	-

shift $\varphi = 2\pi f_{\text{TPPI}}\tau$ was applied, where φ was varied in proportion to τ to introduce an artificial resonance offset of $f_{\text{TPPI}} = 30$ MHz. The longitudinal magnetization was measured as a function of τ (Fig. S6B). The artificial offset increases the sensitivity of the measurement to resonance offsets by allowing more oscillations within the signal decay time constant T_{2e}^* . A fit with an exponential envelope indicates $\delta f = -144$ kHz and $T_{2e}^* = 38(2)$ ns.

To measure the electron spin-lattice relaxation under constant drive $T_{1\rho e}$, the spins were tipped along the x -axis with an adiabatic half-passage (AHP), and then spin-locked with a resonant drive for time τ . An inverse AHP was then applied to bring the spins back to the z -axis. The longitudinal magnetization was measured as a function of τ (Fig. S6C). The $T_{1\rho e}$ obtained from an exponential fit is 2.5(1) ms.

The relaxation measurements on proton spins were done after hyperpolarization for increased SNR. Hence, all associated pulse sequences were preceded by the application of DNP to the electron spins for the optimal build-up time $T_{b,\text{opt}}$ given in the main text.

For proton T_{1p} , the hyperpolarized proton spins were left to equilibrate for time τ (Fig. S6D), after which the longitudinal magnetization was measured. An exponential fit to the data gives $T_{1p} = 10.2(3)$ s.

T_{2p}^* was measured similar to T_{2e}^* for hyperpolarized protons with $f_{\text{TPPI}} = 80$ kHz. The data

(Fig. S6) has a Gaussian decay envelope $\propto e^{-(\tau/T_{2p}^*)^2}$, with $\delta f = 5.2$ kHz and $T_{2p}^* = 17.0(2)$ μ s from the fit. To measure T_{2p} , the spins were tipped to the transverse plane using an AHP, followed by a σ_z decoupling sequence consisting of repeated AFPs separated by a free evolution time $\delta\tau = 5$ μ s. After the decoupling sequence, an AHP inverse was applied to tip the spins back to the z -axis. The total free evolution time $\tau = n\delta\tau$ was varied by incrementing the number n of AFP pulses applied during the decoupling sequence. The longitudinal magnetization was measured as a function of τ (Fig. S6F). An exponential fit to the data gives $T_{2p} = 31.4(7)$ μ s.

6 Thermometry

We calibrate the temperature of the SiNW by measuring the power spectral density (PSD) of displacement fluctuations at the mechanical resonance frequency of the SiNW as a function of the incident laser power. The spectral density of thermal force fluctuations on the SiNW is $S_F = 4k_B k T_{\text{NW}} / (\omega_c Q)$, where k_B is the Boltzmann constant, k is the spring constant, ω_c is the resonance frequency, Q is the native (undamped) quality factor, and T_{NW} is the temperature of the SiNW. We see that the contribution to the displacement PSD from thermal fluctuations is directly proportional to T_{NW} .

In our experimental setup, the entire system is cooled to a base temperature of 4.2 K. However, the laser shining on the SiNW causes sample heating. To determine the excess heating caused by the laser, the following calibration procedure was performed on the 1.3 mM reference sample: First, the sample was positioned 500 nm in the z direction away from the constriction and the feedback damping was turned off. Next, the laser was turned on, and a spectrum analyzer was used to measure the total power in 1) A 5 kHz bandwidth around the NW resonance frequency and 2) A 5 kHz bandwidth in a background region away from the NW resonance frequency. The background power was then subtracted from the total power in order to obtain the thermal displacement power. The integrated displacement power spectral density is plotted

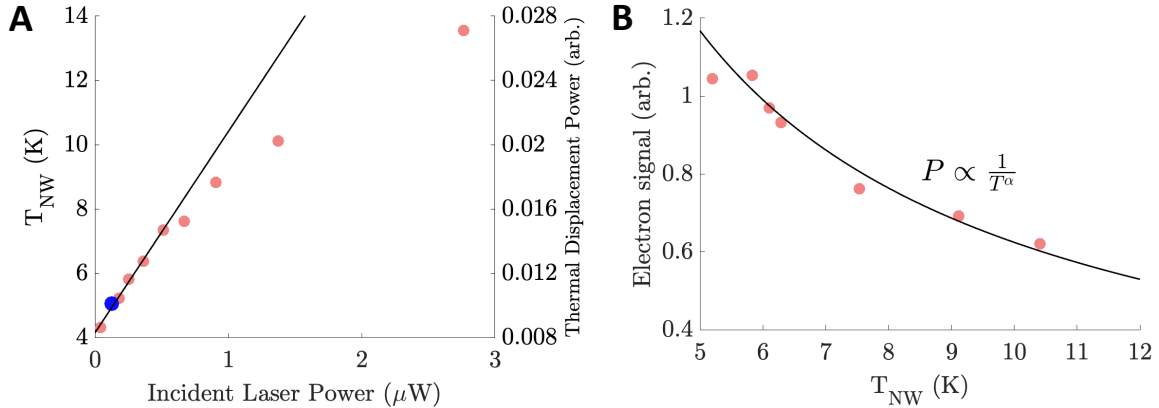


Figure S7: Thermometry Measurements for the 1.3 mM Reference Sample. (A) (right axis) measured thermal displacement power as a function of the incident laser power, (left axis) extrapolated SiNW temperature. The operating light level of the measurements for this sample is indicated by the blue data point. (B) Measurement of the thermal electron spin polarization as a function of the temperature of the SiNW.

as a function of the incident laser power is shown in Fig. S7A. We find that at low light levels, the thermal displacement power increases linearly with the incident laser power. We obtain a calibration of the SiNW temperature by assuming that the y intercept corresponding to the linear part of the curve corresponds to the base temperature of 4.2 K.

As an additional check, we measured the electron spin polarization as a function of the incident laser power. Fig. S7B shows a plot of the electron polarization with the x axis converted to temperature using the data shown in Fig. S7A. We fit the data to a power law $T^{-\alpha}$ and find that the fitted exponent $\alpha = 0.90$ is close to the value $\alpha = 1$, expected from the Curie-Weiss law. Similar measurements on samples A-D revealed a NW temperature of ~ 6 K at the operating light level.

7 Height dependence of bulk T_{1e}

It is known that thermally induced electrical currents (Johnson noise) can cause fluctuating electromagnetic fields close to a conductor, which can increase the spin-lattice relaxation rate (9).

To understand whether proximity to the CFFGS contributed to the enhanced electron spin relaxation, we measured T_{1e} as a function of distance from the CFFGS. Fig. S8B shows the T_{1e} values obtained from the fits to the inversion-recovery curves measured for various tip-surface separations. From the data we conclude that there is no discernible change in T_{1e} caused by proximity to the surface of the CFFGS. The lower SNR for the data measured at 528 nm may be attributed to the decrease in signal resulting from the lower measurement gradients.

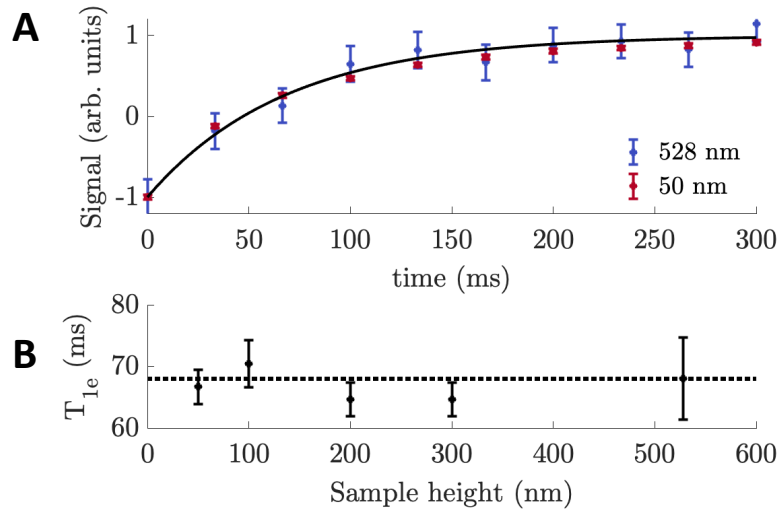


Figure S8: Effect of Sample Height on Measured Bulk T_{1e} . (A) Inversion-recovery curves measured at 50 nm and 528 nm. The black line indicates the fit to a single-exponential decay. Both curves can be fitted by the same $T_{1e} = 70$ ms. (B) T_{1e} vs. tip-surface separation.

8 Data for Sample B, C, and D

Data for the hyperpolarized and thermal time records, the enhanced signal as a function of the build-up time, and the enhanced signal as a function of T_{pol} for various T_{ramp} are shown in Fig. S9, Fig. S10 and Fig. S11.

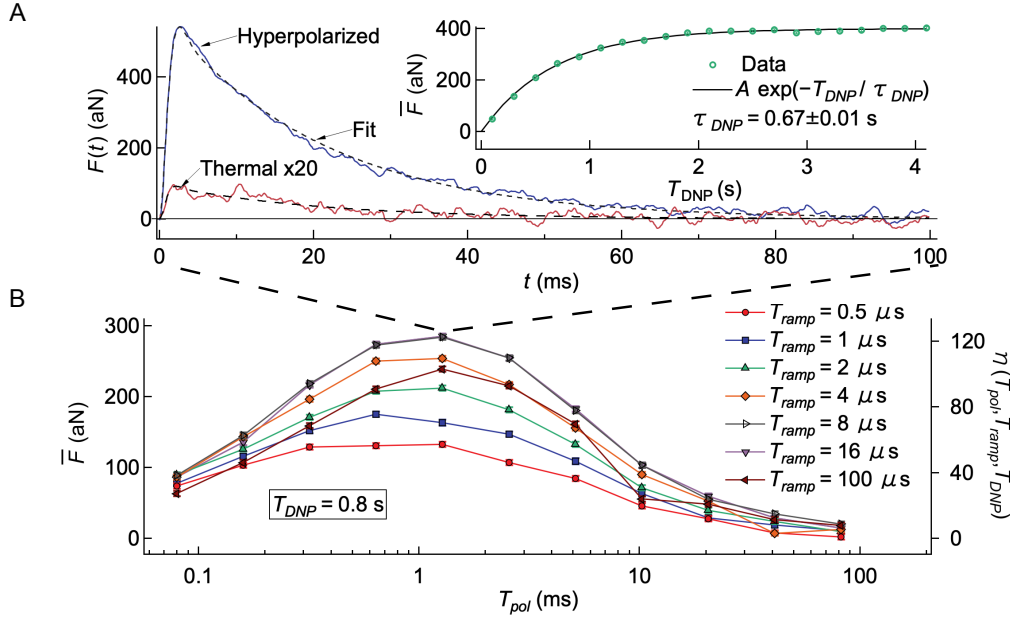


Figure S9: **Sample B Data.** (A) Hyperpolarized and thermal time records. The inset shows the enhanced signal as a function of build-up time. (B) Measured enhancement and enhanced signal as a function of T_{pol} for various T_{ramp} for a build-up time of 0.8 s.

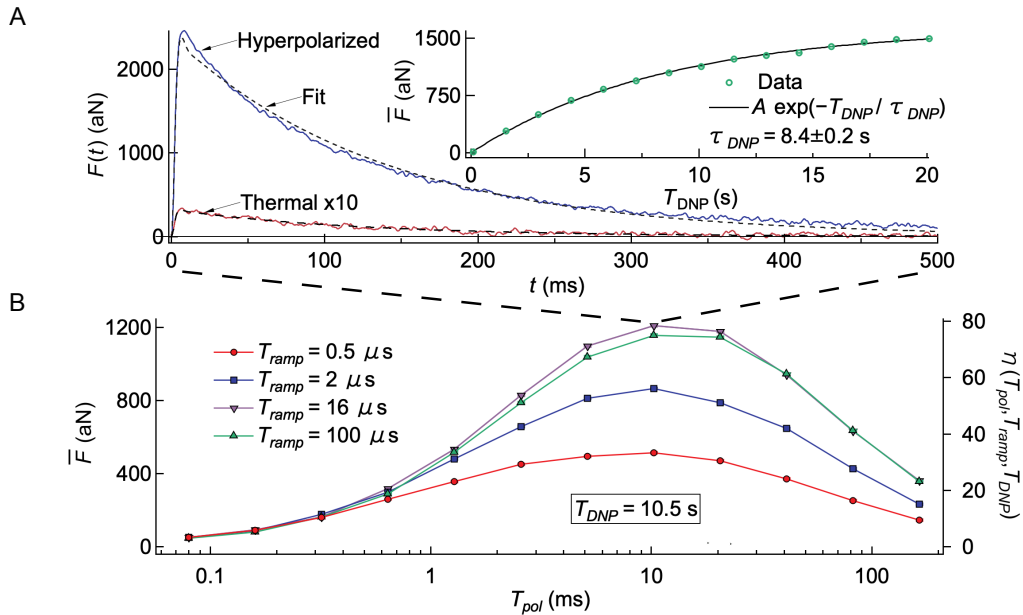


Figure S10: **Sample C Data.** (A) Hyperpolarized and thermal time records. The inset shows the enhanced signal as a function of build-up time. (B) Measured enhancement and enhanced signal as a function of T_{pol} for various T_{ramp} . The build-up time for this sample was 10.5 s.

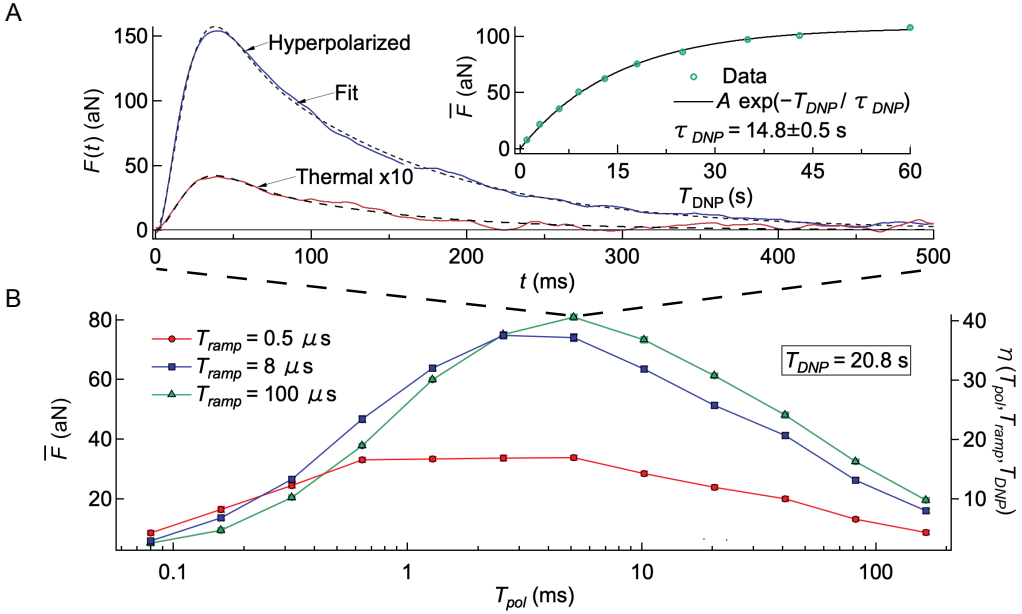


Figure S11: **Sample D Data.** (A) Hyperpolarized and thermal time records. The inset shows the enhanced signal as a function of build-up time. (B) Measured enhancement and enhanced signal as a function of T_{pol} for various T_{ramp} . The build-up time for this sample was 20.8 s.

9 DNP Model

Quantitative understanding of the interplay between the various DNP parameters is essential for optimizing the enhancement. We present a semi-classical model for the polarization transfer process in the limit of perfect adiabaticity. During a DNP sweep, for each electron spin, the model randomly chooses a proton spin to interact with from a uniform probability distribution. The electron will then exchange polarization with that proton. We assume that the electron state at the start of each sweep is statistically independent from the previous one. Denoting the number of spin-up (down) protons and electrons before the sweep by $n_{p\uparrow}$ ($n_{e\uparrow}$) and $n_{p\downarrow}$ ($n_{e\downarrow}$), respectively, the average change in the number of spin-up protons is $\delta n_{p\uparrow} = n_{e\uparrow}n_{p\downarrow}/n_p - n_{e\downarrow}n_{p\uparrow}/n_p$, where n_p is the total number of protons. The average change in the proton polarization due to

the transfer $\delta m_{p,\text{tr}} = \delta n_{p\uparrow} - \delta n_{p\downarrow} = 2\delta n_{p\uparrow}$ is thus given by

$$\delta m_{p,\text{tr}} = \frac{2}{n_p} (n_{e\uparrow} n_{p\downarrow} - n_{e\downarrow} n_{p\uparrow}) = m_e - \frac{n_e}{n_p} m_p, \quad (\text{S19})$$

where m_p and m_e are the total proton and electron polarizations before the sweep, respectively, and n_e is the number of electron spins.

There are two contributions to the change in proton polarization $\delta m_p = \delta m_{p,\text{tr}} + \delta m_{p,\text{rel}}$ between two DNP sweeps: 1) transfer of polarization from the electrons $\delta m_{p,\text{tr}}$, and 2) the relaxation of the protons to the lattice $\delta m_{p,\text{rel}}$. Since $T_{\text{pol}} \ll T_{1p}$, the latter is given by $\delta m_{p,\text{rel}} = m_{p0} + (m_p - m_{p0})e^{-T_{\text{pol}}/T_{1p}} \simeq -(T_{\text{pol}}/T_{1p})(m_p - m_{p0})$, where m_{p0} is the average proton polarization at thermal equilibrium. By combining this with Eq. S19, we find the rate of change for the proton polarization

$$\dot{m}_p(T_b) \simeq \frac{\delta m_p}{T_{\text{pol}}} = - \left(\frac{n_e}{n_p T_{\text{pol}}} + \frac{1}{T_{1p}} \right) m_p(T_b) + \frac{m_e}{T_{\text{pol}}} + \frac{m_{p0}}{T_{1p}}. \quad (\text{S20})$$

Solving Eq. S20 with the initial condition $m_p(0) = 0$ (due to the scrambling pulse), and conversion to the expected force signal gives

$$\bar{F}_{\text{hp}}(T_b, T_{\text{pol}}, T_{\text{ramp}}) = \bar{F}_{\text{th0}} \frac{1 + r(1 - e^{-T_{\text{pol}}/T_{1e}}) \frac{\gamma_e}{\gamma_p} \frac{T_{1p}}{T_{\text{pol}}}}{1 + r \frac{T_{1p}}{T_{\text{pol}}}} (1 - e^{-T_b/\tau_{\text{DNP}}}), \quad (\text{S21})$$

with $r = n_e/n_p$, $\tau_{\text{DNP}} = 1/(T_{1p}^{-1} + rT_{\text{pol}}^{-1})$ is the predicted build-up time constant, and $\bar{F}_{\text{th0}} = \bar{F}_{\text{th}}(T_b \rightarrow \infty)$ is the force signal at thermal equilibrium. Assuming uniform spin densities, r is equal to the electron-to-proton density ratio.

Using Eq. S21, we conduct a simultaneous fit to the T_b - and T_{pol} -dependent data for each sample, with $T_{\text{ramp}} = 100 \mu\text{s}$ to ensure sufficient adiabaticity (Fig. S21D,E). The fit parameters are T_{1e} and r , which are given in Table S3. For both fits, T_{1p} is held constant at the measured value, which is provided in Table 1 of the main text. The fits are in excellent agreement with the data, and the T_{1e} fit value matches the measured T_{1e} for all samples. To contextualize r_{fit} ,

we calculate a range of possible concentration ratios $[r_{\min}, r_{\max}]$ based on the the amount of water remaining in the prepared solution. We observe that for samples B and C, which have the highest OX063 concentrations, r_{fit} falls below the expected minimum r_{\min} . This could be attributed to partial aggregation of OX063 radicals, which can change the spectral properties of the radicals and the number of unpaired electrons. (10, 11).

Table S3: **Semi-classical DNP model fit parameters** $T_{1e \text{ fit}}$, r_{fit} along with the measured T_{1e} and expected proton-to-electron concentration ratios r . Maximum and minimum r values are calculated assuming 0% and 100% water retention in the nanodroplets, respectively.

Sample	A	B	C	D
$T_{1e \text{ fit}}$ (ms)	22.8(3)	2.52(5)	31(1)	23.4(9)
r_{fit} (10^{-5})	51.1(6)	70(2)	47(2)	9.1(4)
T_{1e} (ms)	20.5(3)	2.5(1)	28.6(7)	30.0(4)
r_{\min} (10^{-5})	30.6	82.9	82.9	8.98
r_{\max} (10^{-5})	147	351	351	27.9

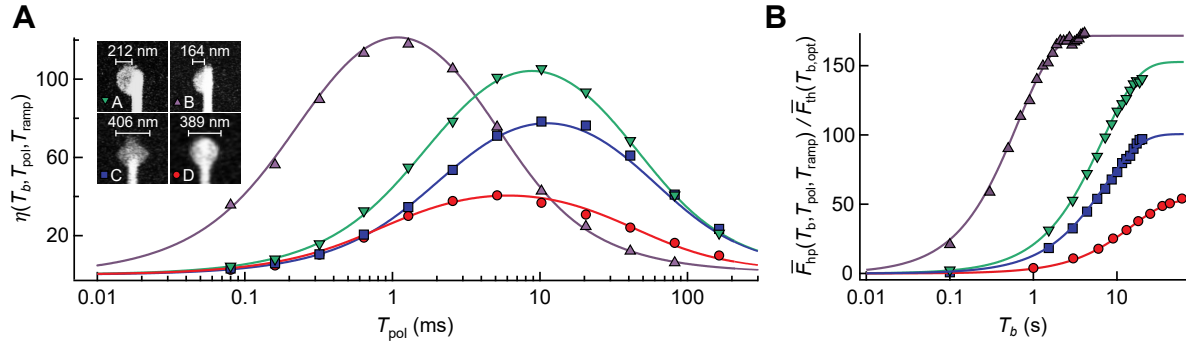


Figure S12: **DNP model fits** for the (A) T_{pol} - and (B) T_b -dependent data. (Inset) SEM images of the nanodroplets attached to each SiNW.

10 DNP-Enhanced and Statistical Polarization SNR Comparison for Sample C

Here, we present the comparison of hyperpolarized and statistical SNRs obtained with sample C. The comparison was conducted in the same manner as for sample A presented in the main text. Fourier encoding using the B_1 gradient was done using the same $10 \mu\text{s}$ resonant pulses discussed in the main text, with the same amplitude sweep. For the hyperpolarized data, the DNP sequence was applied with $T_b = 10.5 \text{ s}$, with $T_{\text{ramp}} = 16 \mu\text{s}$ and $T_{\text{pol}} = 10.24 \text{ ms}$, after which the proton signal was acquired for 500 ms. Each open circles in Fig. S13C, represents the average of two such measurements, corresponding to a total measurement time of 22.13 s. The statistically-polarized data was obtained by evaluating the force correlation for 100 ms measurement blocks. The solid lines in Fig. S13A,C indicate overall average taken over 15.2 h (statistical) and 2.1 h (hyperpolarized). From the data, we determine $\overline{\text{SNR}}_{\text{st}} = 21.99$ and $\overline{\text{SNR}}_{\text{hp}} = 112.05$ for the statistical and hyperpolarized data, respectively, revealing a reduction in averaging time by a factor of $(\overline{\text{SNR}}_{\text{hp}}/\overline{\text{SNR}}_{\text{st}})^2 \times (15.2 \text{ h}/2.1 \text{ h}) = 189$ to achieve the same average SNRs.

11 Simulation of Surface-Induced Spin Lattice Electron Relaxation

In the main text we mention that fast relaxing paramagnetic defects at the Si/SiO₂ interface have a role in the T_{1e} relaxation of the bulk trityl-OX063 radicals. Here, we provide the details of the semi-classical spin diffusion simulation used to investigate the role that paramagnetic defects play. The sample geometry is modelled from scanning electron microscope (SEM) images. A random realization of the spin locations is generated inside the geometry based on the expected concentration of trityl radicals and surface defects. Each spin is assumed to be

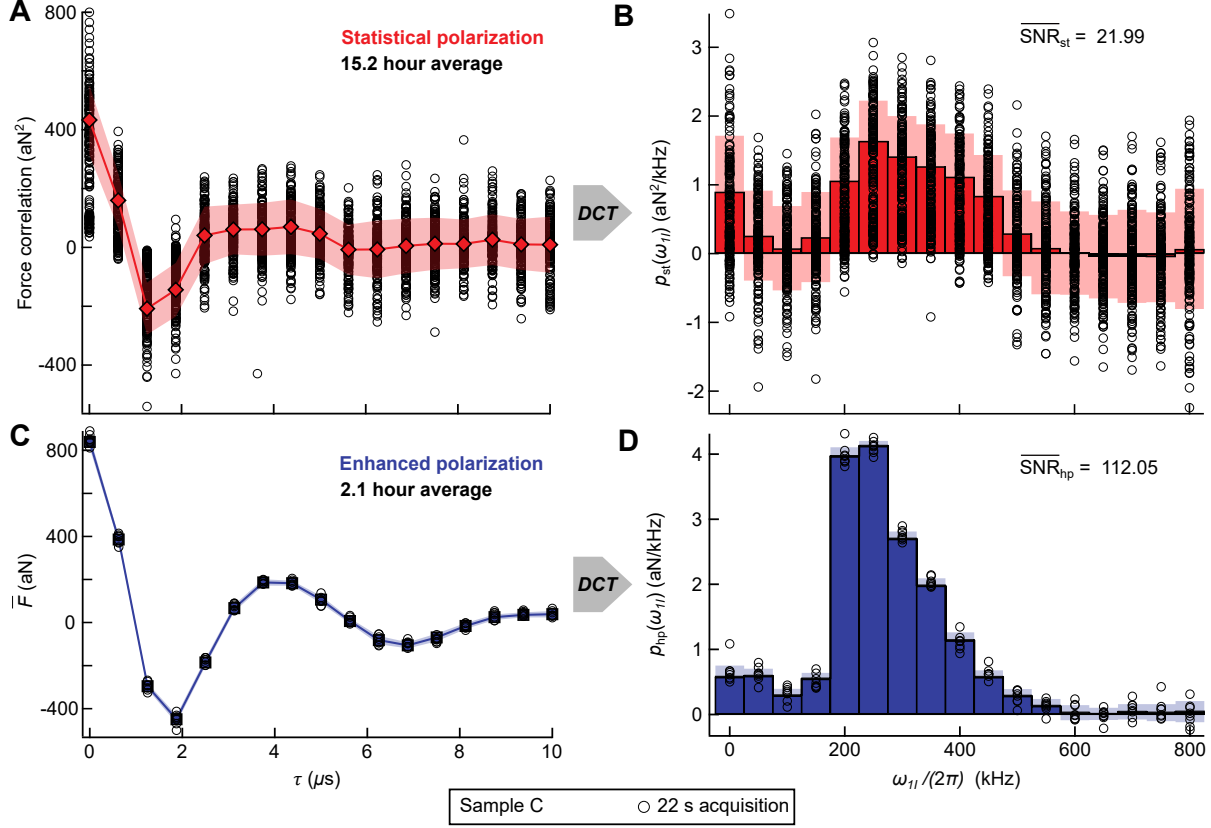


Figure S13: DNP-Enhanced and Statistical Polarization SNR Comparison for Sample C. Measured time-domain Fourier encoding data for (A) statistically-polarized and (C) hyperpolarized proton spins in sample C. The corresponding Rabi frequency distributions are shown in (B) and (D). Similar to the sample A data (Fig. 5 of the main text), the frequency resolution of each distribution is 50 kHz. The shaded regions indicate the standard deviation of the acquired data (open circles) for each point in the time record.

in either an up or down state. We assume that the evolution of each spin is governed by 1) dipole-dipole interactions with neighbouring spins, and 2) the intrinsic spin-lattice relaxation of the trityl radicals and the fast relaxing paramagnetic defects. We calculate the transition rates due to each of these mechanisms through a perturbative approach and probabilistically evolve the spins accordingly. We simulate the measured T_{1e} relaxation process by calculating the gradient-weighted polarization at each time step.

We begin by first modelling our sample geometry, using the SEM images shown in Fig. 2C

of the main text, to approximate the size and location of the SiNWs and the droplets containing the radicals. We generate a random realization of spin locations by mapping a three-dimensional grid of points onto this geometry, taking a grid spacing $\Delta l = 1$ nm. In order to probabilistically populate the grid, we assume that the different points are statistically independent. Each point on the grid is occupied by a spin with a probability of $n_e \Delta l^3$ where n_e is the OX063 concentration presented in Table 3 of the main text, assuming zero water content in the droplet. In the $\Delta l \rightarrow 0$ limit, the spatial distribution approaches a spatial Poisson process with density n_e (12). The fast-relaxing defect spins are assumed to reside in a 1 nm thick layer on the SiNW; the thickness is chosen to approximate the thickness of the Si/SiO₂ interface. The probability of a point on the grid being occupied by a defect is given as $(\sigma_d/1\text{ nm})\Delta l^3$, where σ_d is the defect density. The simulated relaxation curves, shown in Fig. S14, were calculated for values of σ_d in the range of 10^{10} cm⁻² to 10^{14} cm⁻², and different geometries to analyze the role that fast relaxing spins have on spin-lattice relaxation.

A probabilistic approach is taken for modelling the dynamics of the system. Transition rates between spin states are governed by both dipole-dipole interactions between neighboring spins and individual spin-lattice relaxation processes, where the T_{1e} of the bulk spins is assumed to be much longer than those of the fast-relaxing paramagnetic defects. Spin diffusion between electrons is governed by the secular dipolar Hamiltonian which, for a spin pair is $H_D = D(3S_1^z S_2^z - \mathbf{S}_1 \cdot \mathbf{S}_2)$, where $D = \mu_0 \hbar \gamma_e^2 (1 - 3 \cos^2 \theta) / (4\pi r^3)$ in angular frequency units, θ is the angle the static field makes with the line connecting the spin pair and r is the distance between the two spins. We can calculate the transition rates from $|\uparrow\downarrow\rangle \leftrightarrow |\downarrow\uparrow\rangle$ states using Fermi's Golden Rule (13). The transition rate W is calculated as

$$W = 2\pi |\langle \uparrow\downarrow | H_D | \downarrow\uparrow \rangle|^2 \int_{-\infty}^{\infty} d\omega g_1(\omega) g_2(\omega), \quad (\text{S22})$$

where $g_1(\omega)$, $g_2(\omega)$ are the inhomogeneous normalized lineshapes with $\int_{-\infty}^{\infty} d\omega g_i(\omega) = 1$,

$i \in \{1, 2\}$. In the simulation, $g(\omega)$ is taken to be a Lorentzian with a full width at half maximum $\delta\omega = 2/T_{2e}^*$. Assuming the distributions are statistically independent, the transition rate evaluates to

$$W = \frac{D^2}{\delta\omega_1 + \delta\omega_2 + 4\frac{(\omega_{01} - \omega_{02})^2}{\delta\omega_1 + \delta\omega_2}}, \quad (\text{S23})$$

where ω_{01} and ω_{02} are the center frequencies of the bulk and surface spins, respectively, which may be different due to the difference in the distribution of g -factors for the two spin species (14). The probability for a spin to flip in a time interval Δt is $\mathbb{P}(\text{flip}) = W\Delta t$, where Δt is the time step in the simulation. We choose Δt to be sufficiently small, such that the maximum $\mathbb{P}(\text{flip}) \ll 1$, for all spin pairs in the sample. Because the number of spins in the simulated volume can be quite large ($\sim 700,000$), the computation time becomes impractical when considering the interaction for all spin pairs in the sample. We can reduce the computation time considerably by considering the interaction of only those spins within a “sphere of influence”, whose radius is chosen such that the dipole-dipole interaction of the central spin with spins outside the sphere are negligible.

The intrinsic T_{1e} process can also be modelled probabilistically with $\mathbb{P}(|\uparrow\rangle \rightarrow |\downarrow\rangle) = (1 - p_e)\Delta t/T_{1e}$, and $\mathbb{P}(|\downarrow\rangle \rightarrow |\uparrow\rangle) = p_e\Delta t/T_{1e}$ where p_e is the fractional polarization of spins in the up state at 4 K, and T_{1e} is the intrinsic spin lattice relaxation time of the trityl and defect spins measured in bulk concentrations (15, 16, 17).

We assume the initial state of the system to be in a pure state with all spins pointing up. At each time step, we iterate through all spin pairs and calculate the spin-flip probability $\mathbb{P}(\text{flip})$. Then, we generate a random number between 0 and 1. If this number is less than $\mathbb{P}(\text{flip})$ then we flip the states of the spin pair. We then apply the same methodology for a T_1 process using probabilities $\mathbb{P}(|\uparrow\rangle \rightarrow |\downarrow\rangle)$ and $\mathbb{P}(|\downarrow\rangle \rightarrow |\uparrow\rangle)$, with the corresponding T_{1e} for the defect spins and OX063 radicals (15, 16). Table S4 provides the details of the parameters used for simulating

samples A, B, and C as well as the 1.3 mM concentration sample that was used for investigating different electron relaxation mechanisms, referred to as “Reference Sample”. This process is repeated N times with time step $\Delta t = 1\text{ ns}$. At each time step, we calculate and store the gradient-weighted polarization, which is

$$p(t) = \frac{\begin{bmatrix} S_1(t) & \cdots & S_N(t) \end{bmatrix} \begin{bmatrix} G(\mathbf{r}_1) \\ \vdots \\ G(\mathbf{r}_N) \end{bmatrix}}{\sum_{i=1}^N G(\mathbf{r}_i)}, \quad (\text{S24})$$

where $S_i(t) = \pm 1$ refers to the state of the i^{th} spin in the sample at time t . $G(\mathbf{r}_i)$ refers to the detection gradient at the position of the i^{th} spin, and N is the number of spins in the sample.

Table S4: Parameters used for Semi-Classical Spin Diffusion Simulations. Ref. sample refers to the 1.3 mM sample used for investigating different electron relaxation mechanisms.

Sample	A	B	C	Ref. Sample
Intrinsic T_{1e} OX063 (s)	0.1	0.1	0.1	10
Intrinsic T_{1e} defects (μs)	50	50	50	50
OX063 Concentration (mM)	17.8	49.4	49.4	1.3
T_{2e}^* OX063 (ns)	38	27	42	56
T_{2e}^* defects (ns)	12	12	12	12

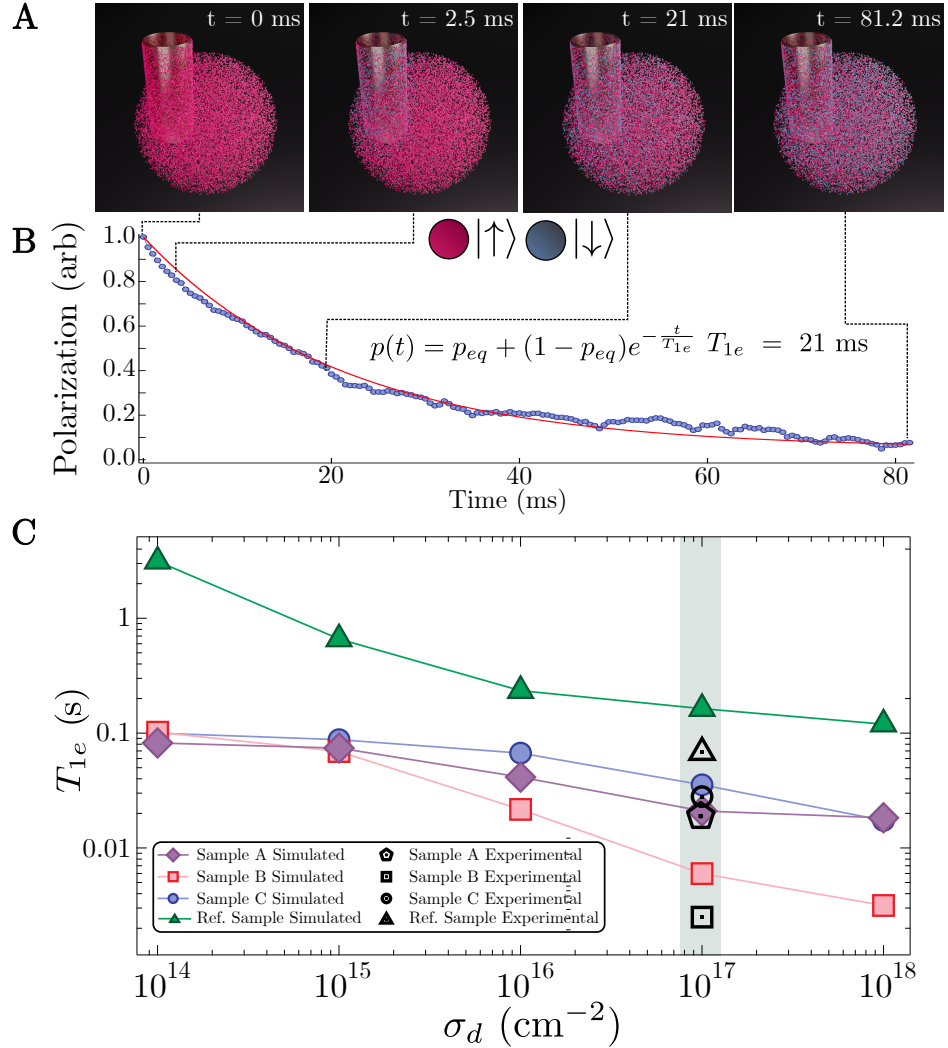


Figure S14: Spin Diffusion Simulation of Surface Induced Spin Lattice Relaxation. (A) Visualization of spin states at different points in T_{1e} decay for Sample A. At $t = 0$, the sample and surface defects are fully polarized. At $t = 2.5$ ms the fast relaxing spins on the surface of the SiNW have reached thermal equilibrium. At $t = 21$ ms, the bulk polarization has reached the $1/e$ point, and we observe an increase in the number of spins in the down state. At $t = 81.2$ ms ($\sim 3T_{1e}$), the sample has reached thermal equilibrium. (B) Sample A fractional polarization time record with spin lattice relaxation time constant $T_{1e} = 21$ ms. (C) Spin-lattice relaxation times for samples A, B, and C and the reference sample for different defect densities on the surface of the SiNW.

The results of the simulation are shown in Figure S14, where we have simulated the T_{1e} relaxation for different NW sample geometries for a range of σ_d . The simulations show good agreement with experimental results for $\sigma_d = 10^{13} \text{ cm}^{-2}$, which is in the range of the expected defect density reported in literature (18, 19, 20, 16). The simulation shows that the presence of fast-relaxing spins of the surface of the SiNW can account for the decrease in T_{1e} of the OX063 radicals observed in our measurements.

12 Experimental Setup and Electronics

Fig. S15 shows a schematic of the experimental setup and electronics used for generating spin control and detection pulses for NMR and ESR. A diode laser operating at $\lambda = 1510 \text{ nm}$ is used to detect the displacement of the SiNW. The light exiting the 5% branch of the fiber coupler is focused to a $1.5 \mu\text{m}$ spot size on the SiNW using a microlens assembly connected to a piezo scanner. The displacement of the SiNW is measured by interfering the back-scattered light from the surface of the SiNW with the light reflected from the cleaved face of the fiber on PD1. The photocurrent generated by PD1 is converted to a voltage using a transimpedance amplifier. The spin signal is obtained by demodulating the voltage signal using a lock-in amplifier referenced to the SiNW frequency (2). The light exiting the 95% branch of the fiber coupler is sent to PD2 which is used to monitor the output of the laser diode. The FPGA shown in the figure is responsible for processing the output of the lock-in amplifier as well as sending timing triggers to the arbitrary waveform generators (AWG) and switches. Spin control pulses employed for the MAGGIC protocol and NMR control are driven differentially through the CFFGS using AWG2 and the RF output of AWG1. AWG2 generates the gradient modulation for MAGGIC at the resonant frequency of the SiNW. Meanwhile, the RF output of AWG1 is used to generate pulses at the Larmor frequency of the protons. The output from AWG2 can be switched on or off to gate the power amplifier used for NMR control pulses. Using a passive filter network,

the signal from AWG1 and AWG2 are combined and routed to the low frequency input of the diplexer, which combines the NMR and ESR pulses. The ESR pulses are generated using a single-sideband IQ mixer to up-convert a baseband signal at 374 MHz from AWG1 to 9.26 GHz. The mixer output is filtered between 9.0 GHz to 9.4 GHz to reduce LO leakage and higher order harmonics. To prevent unwanted relaxation caused by the microwave amplifiers, a fast high-power switch is placed before the diplexer to ensure that the amplifier is only on during the application of microwave pulses.

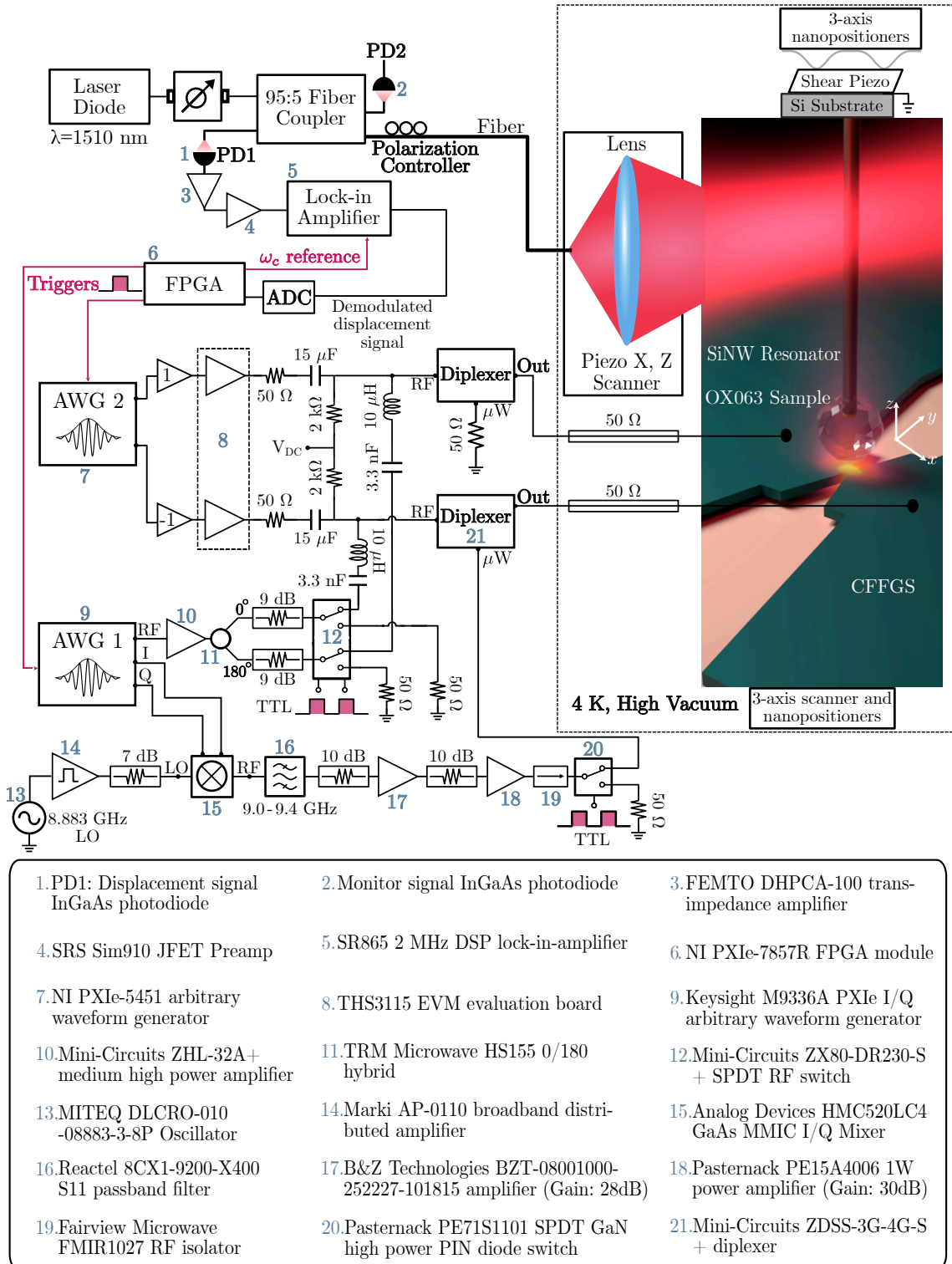


Figure S15: Schematic of the Experimental Setup and Electronics.

References

1. G. Mathies, S. Jain, M. Reese, R. G. Griffin, *Pulsed Dynamic Nuclear Polarization with Trityl Radicals*. *J. Phys. Chem. Lett.* **7**, 111-116 (2016).
2. H. Haas, S. Tabatabaei, W. Rose, P. Sahafi, M. Piscitelli, A. Jordan, P. Priyadarsi, N. Singh, B. Yager, P. J. Poole, D. Dalacu, R. Budakian, *Nuclear Magnetic Resonance Diffraction with Subangstrom Precision*. *Proc. Natl. Acad. Sci. U.S.A* **119**, e2209213119 (2022).
3. W. Rose, H. Haas, A. Q. Chen, N. Jeon, L. J. Lauhon, D. G. Cory, R. Budakian, *High-Resolution Nanoscale Solid-State Nuclear Magnetic Resonance Spectroscopy*. *Phys. Rev. X* **8**, 011030 (2018).
4. S. Tabatabaei, H. Haas, W. Rose, B. Yager, M. Piscitelli, P. Sahafi, A. Jordan, P. J. Poole, D. Dalacu, R. Budakian, *Numerical Engineering of Robust Adiabatic Operations*. *Phys. Rev. Appl.* **15**, 044043 (2021).
5. G. Turin, *An Introduction to Matched Filters*. *IRE Trans. Inf. Theory IEEE* **6**, 311-329 (1960).
6. J. M. Nichol, T. R. Naibert, E. R. Hemesath, L. J. Lauhon, R. Budakian, *Nanoscale Fourier-Transform Magnetic Resonance Imaging*. *Phys. Rev. X* **3**, 031016 (2013).
7. M. B. Priestley, *Spectral Analysis and Time Series*, vol. 1 (1981).
8. M. S. Bartlett, *On the Theoretical Specification and Sampling Properties of Autocorrelated Time-Series*. *J. R. Stat. Soc.* **8**, 27–41 (1946).
9. S. Kolkowitz, A. Safira, A. A. High, R. C. Devlin, S. Choi, Q. P. Unterreithmeier, D. Patterson, A. S. Zibrov, V. E. Manucharyan, H. Park, M. D. Lukin, *Probing Johnson Noise and*

Ballistic Transport in Normal Metals with a Single-Spin Qubit. *Science* **347**, 1129-1132 (2015).

10. I. Marin-Montesinos, J. C. Paniagua, M. Vilaseca, A. Urtizberea, F. Luis, M. Feliz, F. Lin, S. Van Doorslaer, M. Pons, Self-assembled trityl radical capsules – implications for dynamic nuclear polarization. *Phys. Chem. Chem. Phys.* **17**, 5785-5794 (2015).
11. R. Shankar Palani, M. Mardini, Y. Quan, R. G. Griffin, Dynamic nuclear polarization with trityl radicals. *Journal of Magnetic Resonance* **349**, 107411 (2023).
12. A. Papoulis, S. Pillai, *Probability, Random Variables, and Stochastic Processes* (McGraw-Hill, 2002).
13. N. Bloembergen, *On the Interaction of Nuclear Spins in a Crystalline Lattice.* *Physica* **15**, 386-426 (1949).
14. A. Baumer, M. Stutzmann, M. S. Brandt, F. C. Au, S. T. Lee, *Paramagnetic Defects of Silicon Nanowires.* *Appl. Phys. Lett.* **85**, 943-945 (2004).
15. H. Chen, A. G. Maryasov, O. Y. Rogozhnikova, D. V. Trukhin, V. M. Tormyshev, M. K. Bowman, *Electron Spin Dynamics and Spin–Lattice Relaxation of Trityl Radicals in Frozen Solutions.* *Phys. Chem. Chem. Phys.* **18**, 24954-24965 (2016).
16. A. Stesmans, *The .Si Identical to Si₃ Defect at Various (111)Si/SiO₂ and (111) Si/Si₃N₄ Interfaces.* *Semicond. Sci. Technol.* **4**, 1000 (1989).
17. J. Dalibard, Y. Castin, K. Mølmer, *Wave-Function Approach to Dissipative Processes in Quantum Optics.* *Phys. Rev. Lett.* **68**, 580–583 (1992).
18. K. L. Brower, T. J. Headley, *Dipolar Interactions Between Dangling Bonds at the (111) Si-SiO₂ Interface.* *Phys. Rev. B* **34**, 3610–3619 (1986).

19. B. Nouwen, A. Stesmans, *Dependence of Strain at the (111) Si/SiO₂ Interface on Interfacial Si Dangling-Bond Concentration*. *Mater. Sci. Eng., A* **288**, 239-243 (2000).
20. R. Rurrali, *Colloquium: Structural, Electronic, and Transport Properties of Silicon Nanowires*. *Rev. Mod. Phys.* **82**, 427–449 (2010).